2,5-Pyridinedicarboxylic Acid is a Bioactive and Highly Selective Inhibitor of D-Dopachrome Tautomerase

Andrew Parkins[a], Pragnya Das[b], Varsha Prahaladan[b], Vanessa M. Rangel[a], Liang Xue[a], Banumathi Sankaran[c], Vineet Bhandari[b], Georgios Pantouris[a]*

[a] *Department of Chemistry, University of the Pacific, Stockton, CA 95211, USA*

[b] *Division of Neonatology, Department of Pediatrics, The Children's Regional Hospital at Cooper, Camden, NJ 08103, USA*

[c] *Molecular Biophysics and Integrated Bioimaging, Berkeley Center for Structural Biology, 1 Cyclotron Rd, Lawrence Berkeley Nat. Lab, CA-94720*

* **Corresponding Author and Lead Contact**
Georgios Pantouris, gpantouris@pacific.edu

SUMMURY

Macrophage migration inhibitory factor (MIF) and D-dopachrome tautomerase (D-DT) are two pleotropic cytokines, which are coexpressed in various cell types to activate the cell surface receptor CD74. Via the MIF/CD74 and D-DT/CD74 axes, the two proteins exhibit either beneficial or deleterious effect on human diseases. In this study, we report the identification of 2,5-pyridinedicarboxylic acid (a.k.a. **1**) that effectively blocks the D-DT induced activation of CD74 and demonstrates an impressive 79-fold selectivity for D-DT over MIF. Crystallographic characterization of D-DT-**1** elucidates the binding features of **1** and reveals previously unrecognized differences between the MIF and D-DT active sites that explain the ligand's functional selectivity. The commercial availability, low cost, and high selectivity make **1** the dels. At the

same time, our comprehensive biochemical, computational, and crystallographic analyses serve as a guide for generating highly potent and selective D-DT inhibitors.

INTRODUCTION

Understanding the correlation between protein expression and disease progression is laborious as it requires in depth investigation of mechanistic pathway(s) using a well-designed experimental study. If the same activity is shared among multiple proteins, then the task is even more challenging and demands the use of selective modulators. A representative example of such proteins is MIF and D-DT; the two human members of the MIF superfamily that are coexpressed in various cell types and tissues and share a cytokine [1,2], tautomerase [3,4], and endonuclease [5,6] activity.

MIF was originally reported in the 1960s as an "inhibitory factor" of random macrophage migration produced by T-cells [7], but was later on also detected in a variety of immune cells and nearly every tissue [8]. The MIF signal transduction network is complicated and involves biological partners found on the cell surface as well as intracellularly. The most well-studied protein partners are the CD74/CD44 complex [2,9], which serves as the canonical MIF receptor, and non-canonical chemokine receptors CXCR2, CXCR4, and CXCR7 [10,11]. The MIF induced activation of CD74/CD44, chemokine receptors, or the CD74/CXCR heterogenic complexes (CD74/CXCR2 [10], CD74/CXCR4 [12], and CD74/CXCR4/CXCR7 [11]) occurs in either an autocrine or paracrine fashion, depending on the stimulus and cell type. Subsequently, the mitogen-activated protein kinase (MAPK)/extracellular signal-regulated kinase (ERK), phosphoinositide 3-kinase (PI3K)-protein kinase B (AKT), and/or AMP-activated protein kinase (AMPK) signaling pathways are activated with downstream effects that regulate cell growth, proliferation,

and inhibition of apoptosis. Under pathological conditions, these signal transduction events will advance a variety of disorders, including inflammatory diseases [13] and cancer [14]. The expression level of MIF in these conditions is highly influenced by the gene's promoter polymorphisms. For example, a 5-8 repeated sequence of CATT tetranucleotide at position -794 of the human *Mif* gene has been associated with disease severity for patients with rheumatoid arthritis [15]. Besides the expression levels of MIF, recent clinical findings obtained from patients with inflammatory diseases [16] and cancer [17] have shown that the pathogenic action of MIF is also related to a unique structural isoform of the protein found only in oxidized environment. The oxidized structural isoform of MIF [18], also known as oxMIF, is exclusively detected in inflammation and cancer and serves as an attractive molecular target and diagnostic tool for these pathological conditions.

Structurally, MIF is composed of only 114 amino acids forming a homotrimeric biological assembly. The MIF trimer possesses a solvent channel at the center, and an enzymatic pocket in the interface of two monomers [19]. Pro1, which is located at the edge of this pocket, is responsible for the tautomerase activity of MIF. Via this activity, a large number of MIF modulators have been discovered and characterized including competitive [20], non-competitive [21], and covalent inhibitors [22]. Among the numerous MIF inhibitors reported thus far, only 4-iodo-6-phenylpyrimidine (4-IPP) is known to inhibit the activity of D-DT, by creating a covalent adduct with the catalytic residue Pro1 [23].

D-DT is the second human member of the MIF superfamily that shares a high structural homology [24] yet a low sequence identity (only 34%) with MIF [1]. Although D-DT was cloned and crystallized in the 1990s [24], its functionality has not been extensively studied due to the belief that it is the product of *Mif* gene duplication [25]. Nevertheless, growing evidence has shown that D-DT expression has a non-redundant functionality in inflammation, autoimmune diseases,

cardiovascular disorders, and cancer [26]. In some pathological conditions D-DT may act cooperatively/synergistically with MIF, while in others the two proteins have different or even oppositional activities. Cooperative action of MIF and D-DT has been reported in various types of cancer [27], inflammatory disorders including sepsis [1] and chronic obstructive pulmonary disease [28], and heart conditions such as cardiac ischemia/reperfusion injury [29,30]. In contrast, studies on adipose tissue inflammation [31] and systemic sclerosis [32] demonstrate that the expression of D-DT and MIF serve two distinct functional roles.

Whereas the MIF functionality is associated with activation of multiple receptors and receptor complexes, D-DT is mainly mediated by the CD74/CD44 receptor complex [1]. The D-DT/CD74 interface has yet to be defined, but previous results have shown that a D-DT tautomerase inhibitor can effectively block activation of the receptor [33]. Upon the formation of the homotrimeric assembly, the active site pocket of D-DT is positioned in the interface of two monomers, similar to MIF [24]. Despite sharing the tautomerase activity, MIF and D-DT have noticeable differences in the amino acid composition of their active sites. Consequently, the large number of MIF inhibitors are ineffective on D-DT and only two reversible inhibitors are so far known for the latter protein [33,34]. The first inhibitor, called 4-(3-carboxyphenyl)-2,5-pyridinedicarboxylic acid (4-CPPC), was identified recently by an *in-silico* screen of 1.6 million compounds [33]. The second D-DT inhibitor, (R)-5-Methyl-3-(1-(naphthalen-1-yl)ethyl)-6-(3-(trifluoromethyl)phenyl)thieno[2,3-d]pyrimidine-2,4(1H,3H)-dione was discovered via the screening of 305 compounds from an in house collection [34]. In both cases, the inhibitors revealed micromolar inhibition potencies and low to moderate selectivity for D-DT over MIF.

In this study, we describe the identification and characterization of 2,5-pyridinedicarboxylic acid (**1**) as a commercially available, bioactive, and highly selective

inhibitor of D-DT. Enzymatic assays demonstrate that **1** has a 79-fold inhibition selectivity for D-DT over MIF. Notably, this compound has the highest selectivity among the known D-DT inhibitors. Crystallographic analysis of D-DT-**1** and side-by-side comparison with known MIF crystal structures expose key structural differences between the MIF and D-DT active sites that were previously unseen. These new findings provide insights into the regulation of ligand binding by MIF and D-DT, and clarify the inhibition selectivity criteria. The identification of **1** would aid the efforts towards understanding the biological activity of D-DT in disease models and clinical samples as well as the development of new generation D-DT modulators that target activation of CD74.

RESULTS

Identification of 1 as a highly selective inhibitor of D-DT. Analysis of the D-DT-4-CPPC co-crystal structure suggested the benzoic acid moiety was redundant due to the lack of stabilizing interactions with active site residues [35]. To experimentally verify this structural observation and gain mechanistic insights into inhibition of D-DT, we purchased selected 4-CPPC derivatives and performed single point kinetic assays on both D-DT and MIF (**Figs. 1A, 1B**). **1** was generated by deletion of the m-Toluic acid group in 4-CPPC, while a nitrogen to carbon substitution in the pyridine ring produced **2** (terephthalic acid) (**Fig. 1C**). Removal of either 2- or 5-carboxylate group produced **3** (pyridine-2-carboxylic acid) and **4** (nicotinic acid), respectively. Finally, **5** (4-phenylpyridine) was produced by elimination of the three carboxylate groups in 4-CPPC. We projected that these structural modifications of 4-CPPC, would provide key information for the development of new D-DT inhibitors. The single point screening strategy, at a testing concentration of 100 μM, was chosen over a multipoint kinetic assay due to the moderate inhibition potency of 4-CPPC [33,35]. At the same time, we anticipated that the stepwise

removal of functional groups from 4-CPPC (**Fig. 1C**) would only have a negative impact on the inhibition potency of the produced molecule, thus a high testing concentration of each compound would be required.

The five compounds along with 4-CPPC were tested against D-DT (**Fig. 1A**) and MIF (**Fig. 1B**) to determine inhibition potency and selectivity. For our experiments 4-CPPC, with a previously reported K_i of 33 ± 0.7 μM [35], served as a reference D-DT inhibitor (positive control). As a negative control, we used dimethyl sulfoxide (DMSO) at a final concentration of 1%. In comparison to 4-CPPC, **1** had an improved inhibition potency and retained selectivity for D-DT (**Figs. 1A, 1B**). At the single concentration of 100 μM, 4-CPPC and **1** inhibit the activity of D-DT by 53% and 77%, respectively. The negligible inhibition potencies of **2-5** against D-DT, demonstrate that the nitrogen atom and two carboxylate groups of the pyridine ring serve a key role in the inhibition potency of **1** (**Fig. 1A**). Similar to 4-CPPC and **1**, compounds **2-5** are inactive against MIF (**Fig. 1B**).

We carried out multipoint kinetic experiments against D-DT and MIF to quantitatively determine the inhibition potency and selectivity of **1** (**Fig. 2**). The single point kinetic data (**Fig. 1A, B**) guided the design of these experiments and determine the appropriate concentration ranges of **1**. For D-DT, **1** was tested at a concentration range of 0-50 μM. In the case of MIF, we had to do several preliminary kinetic trials before we finalized the concentration range between 0-3000 μM. We noticed absorbance inconsistencies, when **1** tested at concentrations >600 μM. This finding aligns with the previously described property of **1** to form complexes with solution ions (e.g. Zn, Ni, Cu, and Fe) [36], and it was resolved by the use of 1 mM ethylenediaminetetraacetic acid (EDTA). The K_i values of 17.2±0.9 μM and 1360±297 μM were obtained for D-DT and MIF, respectively (**Fig. 2**). **1** demonstrates an impressive 79-fold

selectivity for D-DT over MIF. In contrast to 4-CPPC [35], the inhibition potency and selectivity of **1** for D-DT was improved by 2- and 6-fold, respectively.

Structural characterization of D-DT-1. We probed crystallographic characterization of the D-DT-**1** complex, to provide structural evidence of the compound's inhibition activity and selectivity. We employed isothermal titration calorimetry (ITC) and circular dichroism (CD) spectroscopy, prior to setting up crystallization trays, in order to determine the binding affinity of **1** and thermal stability of D-DT-**1**, respectively. Our ITC findings demonstrate a 1:1 protein to ligand stoichiometry with a dissociation constant (K_D) of 36 μM (**Fig. S1**). Next, we ran thermal denaturation experiments of apo D-DT and D-DT-**1**. To ensure all active sites were fully occupied, we recorded the melting profile of D-DT-**1** three times at ligand concentrations multiple folds above the K_D value (**Fig. S1**). The melting temperature of apo D-DT was determined at 71 ^oC, whereas the ligand did not have a noticeable effect on the stability of the protein (**Fig. S2**).

Given the modest K_D value, we did not attempt co-crystallization of D-DT with **1**. Instead, we produced apo D-DT crystals and soaked them in 100 mM of **1**. Through this approach, the D-DT-**1** crystal structure was obtained (**Table 1**) and the electron density of **1** was clearly detected in all three active sites (**Fig. 3A, Fig. S3**). The structural impact of D-DT-**1** complex formation was examined at a global (trimeric D-DT) and local (active site) level with the known structure apo D-DT (Protein Data Bank (PDB) entry: 1DPT [24]) as the point of reference. At a global level, D-DT-**1** and apo D-DT demonstrated negligible structural differences, with a root-mean-square deviation (RMSD) value of 0.33 Å (**Fig. 3B**).

Binding of **1** did not trigger any major conformational changes in the active site as we have previously seen with 4-CPPC [35] and the C-terminal adopted a structural orientation similar

to that of apo D-DT (**Fig. 3B**). Upon comparison with apo D-DT (**Fig. S4A**), we found that the active site opening of D-DT-**1** was noticeably enlarged (**Fig. S4B**). Our observation agrees with previous crystallographic findings [33] and is associated with the ligand-induced conformational change of Arg36. This gating residue is located at the opening of the active site, positioned in two distinct conformations depending on the protein's state. The "closed" conformation of Arg36 was noted in the apo D-DT structure and resulted in a narrow active site opening that does not physically allow any molecules to enter the pocket (**Fig. S4A**). However, in the presence of an active site binder such as **1**, the side chain of Arg36 adopts a different conformation that increases the opening of the pocket and permits ligand binding (**Fig. S4B**).

Hydrogen bonding and electrostatic interactions are the main stabilizing forces of D-DT-**1** (**Fig. 3C**). Hydrophobic interactions also contribute to the stability of the complex albeit to a lesser extent. The two carboxylate groups of **1** form hydrogen bonds with Pro1, Lys32, Ser63, Ile64, and Lys109 and electrostatic interactions with Lys32, Arg36 and Lys109 (**Fig. 3C**). The carboxylate group, at position two, plays a central role in binding by forming four hydrogen bonding interactions with active site residues. The second carboxylate group, at position five, promotes binding of **1** due to electrostatic interactions for the most part (**Fig. 3C**). Our crystallographic analysis and single point kinetic results support that neither of the carboxylate groups would be able to orient correctly in the active site of D-DT if the pyridine nitrogen is missing (**Figs. 1A, 3C**). Hydrophobic interactions involving Pro1, Ser63 and Ile64, play a weak but supportive role in stabilizing D-DT-**1**.

Analysis of D-DT-1 profile by MD simulations. Along with the conformational change of Arg36, which controls ligand binding via regulation of the active site opening, we have previously brought to light an induced-fit mechanism that involved C-terminal conformational

changes upon 4-CPPC binding [35]. Consequently, the residues M114-L117 became unusually flexible resulting in elimination of their electron densities. These findings uncover structural features of D-DT that noticeably differ from what we know for MIF and aid the efforts towards understanding the structure-function aspects of the MIF superfamily members.

We employed MD simulations to examine how **1** influences the intra- (within monomer A) and intersubunit (monomer A with monomers B and C) communications of D-DT. The duration of each calculation was 200 ns and the produced correlation plots of apo D-DT and D-DT-**1** were compared side-by-side (**Figs. 4A, 4B**). The extent of correlation between two given regions is graphically measured on a scale of 0 to 1. Green, blue, orange, and red colors represent regions with none to low, low to moderate, moderate to strong, and strong to absolute correlation, respectively (**Figs. 4A, 4B**). The absolute correlation value equates to 1 and is obtained only when a residue is compared to itself. Distal correlated regions, illustrated in orange, are the most interesting for further assessment. From this analysis, we found **1** has an overall negative impact on the intra- and intersubunit correlations of D-DT. Graphically, this is illustrated in the apo D-DT (before binding) and D-DT-**1** (after binding) correlation plots as a color change from either orange to blue (white circle and boxes) or blue to green (yellow circle and boxes) (**Figs. 4A, 4B**). Moderate to low correlation changes (yellow circle and boxes) have only a qualitative value of global reduction of communications, thus, these regions would not undergo further analysis. In contrast, the strong to moderate correlation changes (white circle and boxes) highlight interruption of key intra- and intersubunit communications. Such correlation changes would be analyzed in detail because they serve as a tool to understand the inhibition features of **1**.

One intrasubunit (55-64 A with 93-103 A) and two intersubunit (66-77 A with 112-117 B and 111-117 A with 66-76 C) correlations were significantly affected by the formation of D-DT-**1** complex (**Figs. 4A, 4B**). After mapping these regions on the crystal structure of D-DT-**1** (**Fig. 4C**), we probed for crystallographic evidence to explain the correlation results. We found that Ser63, Ile64, and Lys109, which form hydrogen bonding interactions with **1** (**Fig. 3C**), possess key positions on the affected segments. Ser63 and Ile64 are located on β4 strand and α2/β4 loop, respectively. Restriction in their molecular motions, due to hydrogen bonding with **1**, has a direct impact on the conformational flexibility of β4 strand. Consequently, the intrasubunit correlation between segments 55-64 and 93-103 of subunit A, is also affected (**Fig. 3C**). Lys109 is located on a key position of the C-terminal, like Ser63 and Ile64. Hindering the mobility of Lys109 due to hydrogen bonding with the ligand, influences the ability of the C-terminal to effectively communicate with the α2 helix from the adjacent monomer.

To assess the impact of ligand binding in protein dynamics, we calculated root mean square fluctuation (RMSF) of apo D-DT and D-DT-**1** and overlaid the two plots (**Fig. S5**). At a global level (D-DT trimer), we noted negligible differences with an average RMSF value of 0.62±0.2 Å and 0.58±0.2 Å for D-DT and D-DT-**1**, respectively. At a local level (active site pocket), we detected noticeable shifting in the fluctuation activity of two regions. After structural mapping, we found that the two affected segments, 24-36 and 64-69, are located proximal to the binding site of **1**. Upon complex formation, Lys32, Arg36, and Ile64 establish electrostatic (Lys32 and Arg36) and hydrogen bonding (Il64) interactions with **1** (**Fig. 3C**), leading to reduction of 24-36 and 64-69 segments' flexibility.

Structural basis of ligand recognition and functional selectivity. The multipoint kinetic results showed an impressive selectivity of **1** for D-DT (**Fig. 2**). To clarify the parameters of this

selectivity, we performed a structural analysis focusing on the ligand recognition features of D-DT and MIF. The active site volumes of apo MIF (magenta), apo D-DT (grey), and D-DT-**1** (blue) (**Fig. 5**) were calculated and compared using pyVOL, a PyMOL plugin for visualization, comparison, and volume calculation of ligand binding sites [37]. Numerically, the active site volume of apo MIF is the smallest of all three, with an average value of 175±4 Å^3. In the absence of a ligand, the average volume of D-DT was calculated at 203±1 Å^3, while in the presence of **1**, it increased to 210±0 Å^3 due to the conformational change of Met114 (**Fig. S6**). Conformational changes of Lys32 and Arg36 enabled stabilizing interactions with **1** (**Fig. 3**), but they are not accountable for the increase of volume.

Structural alignment of apo MIF and D-DT displayed a perpendicular orientation of the two active site pockets (**Fig. S7**). This finding shows that the structural basis of ligand recognition for each protein is significantly different. The significance of this discovery is better understood by comparing the binding orientations of **1** and 4,5-Dihydro-3-(4-hydroxyphenyl)-5-isoxazoleacetic acid methyl ester (ISO-1) in the corresponding active site pockets of D-DT and MIF (**Fig. 6**). ISO-1 is widely used for *in vitro* and *in vivo* experiments as a proof-of-concept MIF therapeutic [38]. In this study, ISO-1 was chosen as a representative MIF inhibitor based on our crystallographic analysis, which showed this molecule accurately represents the binding orientation of MIF ligands with diverse chemical scaffolds (**Fig. S8**).

Upon comparing the binding features of **1** and ISO-1 (**Fig. 7**), we found key structural differences that explain the high selectivity of **1** for D-DT; the first being the conformational flexibility of residue two. For MIF and D-DT, residue two is a Met and Phe, respectively (**Fig. 7A**). The crystal structures of apo MIF [39] and MIF-ligands [40] demonstrate that the side chain of Met2 is highly flexible and adopts multiple conformations. The enhanced flexibility of this

residue allows MIF to accommodate ligands in binding orientations like that of ISO-1 (**Fig. 6, Fig S8**). For D-DT, this is excluded due to the presence of Phe2 (**Fig. 7A**). The conformational flexibility of residue 36 is another regulatory point, which provides mechanistic evidence in relation to MIF and D-DT ligand selectivity (**Fig. 7B**). This residue possesses a dual functional role of ligand recognition and stabilization. For MIF, the conformational changes of Tyr36 do not have a noticeable impact on ligand binding (**Fig S8**). Instead, the primary role of such movements is to enable interactions with the ligand and promote stabilization of the MIF-ligand complex [41]. Arg36 also contributes to ligand stability in D-DT (**Fig. 3C**), however, the predominant functional role of its conformational change is to enable ligand binding by enlarging the size of the active site opening (**Fig. S2**). The MIF pocket contains multiple aromatic residues that not only increase the hydrophobicity of the pocket, but also define the shape of the pocket (**Fig. 7C**). Thus, in relation to Pro1, a ligand like **1** would clash due to the requirement of binding in a vertical geometry.

Inhibition of D-DT induced activation of CD74 by 1. Following the biochemical, computational, and structural characterization of D-DT-**1**, we probed whether **1** inhibits the D-DT induced activation of CD74. To avoid *in vitro* complications related to the stability of the receptor [42], we utilized a previously established *in vivo* assay that accurately measures the MIF or D-DT induced activation of CD74 [22,23,43-47]. The principle of this neutrophil recruitment assay is based on the ability of lipopolysaccharides (LPS)-free MIF or D-DT to activate CD74 on the cell surface of bronchoalveolar lavage (BAL) macrophages. Upon activation of CD74, the proinflammatory proteins macrophage-inflammatory protein 2 (MIP-2) and keratinocyte chemoattractant (KC) are recruited, which in turn trigger accumulation of neutrophils within the

period of 4-6 hours [43]. The number of neutrophils found in the alveolar space determines the extent of CD74 activation.

For this assay, **1** was intratracheally installed in the lungs of mice at a concentration range of 10-40 μM. This range was chosen considering the K_i (**Fig. 2**) and K_D (**Fig. S1**) values of D-DT-**1**, as well as the potential lethality risk in the case of using higher concentrations of **1**. The inhibitor was installed in the presence or absence of D-DT, having saline as a negative and apo D-DT as a positive control. Testing **1** in the absence of D-DT, would determine if the compound itself has inflammatory properties. Intratracheal installation of apo D-DT resulted in an increase of BAL proteins that is significantly different from the remaining experimental groups (**Fig. 8A**). In contrast, the saline group did not have a noticeable impact on recruiting BAL proteins. Together, these findings show the experiment followed the anticipated mechanistic pathway [43], which was the accumulation of proinflammatory proteins upon the D-DT-induced activation of CD74. While the concentration of BAL proteins is not an accurate measurement of CD74 activation, we also calculated neutrophils (**Fig. 8B**). As shown by the saline group, neutrophils are not present in the alveolar space; instead, they are recruited upon installation of D-DT. The significant elevation of neutrophils, noted in the case of apo D-DT (**Fig. 8B**), was blocked in the presence of 10-40 μM of **1**. At the same time, the compound itself has minor inflammatory properties.

DISCUSSION

Highly promising protein modulators with impressive therapeutic results at preclinical models, often hit a roadblock in clinical trials [48]. Among the reasons contributing to the negative outcome are the incomplete understanding of the protein's molecular mechanisms and the compensatory

expression of homologs that share the same biological activity [49]. The two human members of the MIF superfamily, D-DT and MIF, share the most notably cytokine activity [1,2] as well as endonuclease [5,6] and tautomerase [3,4] activities. The early identification of MIF as an immunomodulatory protein garnered much interest towards resolving its biological activity, ignoring at the same time the existence of D-DT. Several studies have shown D-DT has a regulatory function in immunity [1,50], though an in-depth understanding of its functionality, in human physiology and pathology, is still missing. One could attribute that this is partially due to the lack of highly selective D-DT modulators that can be utilized alongside the abundant MIF inhibitors.

In this study, we report the identification and characterization of **1** as a highly selective inhibitor of D-DT, providing at the same time the structural basis of this selectivity. Kinetic experiments revealed a 79-fold selectivity of **1** for D-DT over its human homolog MIF, while a neutrophil recruitment assay demonstrated that the compound is an effective *in vivo* inhibitor of the CD74 activation. The micromolar inhibition potency (17.2±0.9 μM) of **1** for D-DT leaves room for improvement, but without shadowing its importance as the D-DT inhibitor with the highest selectivity reported thus far. A careful examination of the literature shows that ISO-1, which is the most utilized MIF inhibitor for *in vitro*/*in vivo* MIF studies, has inhibition (K_i) and dissociation constants (K_D) equal to 24.1±1.7 μM and 14.4±2.3 μM, respectively [21]. ISO-1 and **1** may concurrently be used to elucidate the precise biological functionality of MIF and D-DT, in cell types and tissues that the two proteins are coexpressed.

A side-by-side comparison of **1** with the two previously reported, selective inhibitors of D-DT demonstrate the clear advantages of this compound. Starting with 4-CPPC, **1** has a 2- and 6-fold improved inhibition potency and selectivity, respectively [35]. While neither the inhibition

constant of 4-CPPC (33±0.7 μM) nor **1** (17.2±0.9 μM) make the two molecules drug candidates, the improved D-DT/MIF selectivity of the latter (4-CPPC:13-fold selectivity versus **1**:79-fold selectivity), make it more suitable for mechanistic studies. The conformational changes observed at the C-terminal of D-DT as a consequence of 4-CPPC binding are of unknown significance, but it is important to note that in the case of **1**, the C-terminal remains unaffected. Besides the functional aspects, **1** has additional advantages related to its cost and availability. **1** is broadly available in the market at a much lower price than 4-CPPC, which is offered only by selected manufacturers. In regards to the second known inhibitor of D-DT [34], (R-5-Methyl-3-(1-(naphthalen-1-yl)ethyl)-6-(3-(trifluoromethyl)phenyl)thieno[2,3-d]pyrimidine-2,4(1H,3H)-dione), **1** also has multiple advantages. Besides the fact that the compound is not commercially available, it has also a much lower selectivity for D-DT (>50-fold selectivity). Unfortunately, the inhibition potency of this inhibitor cannot be directly compared to the corresponding value of **1** due to usage of different substrates. Collectively, our findings demonstrate that **1** is an attractive tool for interrogating the biological activity of D-DT in various disease models and clinical samples.

ACKNOWLEDGMENTS

This work was supported by start-up funds from University of the Pacific and Scholarly/Artistic Activities Grant (G.P.). The Berkeley Center for Structural Biology is supported in part by the Howard Hughes Medical Institute. The Advanced Light Source is a Department of Energy Office of Science User Facility under Contract No. DE-AC02-05CH11231. The ALS-ENABLE beamlines are supported in part by the National Institutes of Health, National Institute of General Medical Sciences, grant P30 GM124169. The purchase of an isothermal titration calorimeter is supported by the National Science Foundation (MRI-1828179).

AUTHOR CONTRIBUTIONS

A.P. expressed and purified proteins, carried out the CD and kinetic, performed the MD simulations, crystallized D-DT-**1** and refined the structure, analyzed data, wrote, and edited the manuscript. **P.D.** and **V.P.** performed the *in vivo* experiments, analyzed data, and contributed to the writing of the manuscript. **V.R.** performed the ITC experiments and contributed to the writing of the manuscript. **L.X.** supervised the ITC experiments and edited the manuscript. **B.S.** collected the D-DT-**1** data set. **V.B.** supervised the in vivo experiments, analyzed data, and edited the manuscript. **G.P.** conceived, supervised the project, analyzed data, wrote, and edited the manuscript. All the authors have given approval to the final version of the manuscript.

DECLARATION OF INTEREST

The authors declare no competing interests.

INCLUSION AND DIVERSITY

We support inclusion, diverse, and equitable conduct of research.

FIGURE LEGENDS

Figure 1. **Percent activity of D-DT and MIF by 4-CPPC derivatives**. The tautomerase activities of (**A**) D-DT and (**B**) MIF were tested in the presence of 4-CPPC derivatives (**C**) at the single concentrations of 100 μM and 1 mM for the 4-CPPC derivatives and 4-HPP, respectively. 100% activity corresponds to the average value of the non-inhibited reaction. The experiments were carried out in triplicate (n=3) and the error values are shown as standard deviations (SD).

Figure 2. **Kinetic characterization of 1 against D-DT and MIF**. The inhibition activity of **1** against D-DT and MIF was examined at the concentration ranges of 0-50 μM and 0-3000 μM, respectively. The experiments were carried out in triplicate (n=3) and the error values are shown as standard deviations (SD).

Figure 3. **Crystallographic characterization of D-DT-1**. (**A**) The *2Fo-Fc* electron density of **1** was clearly observed in the three active sites of D-DT. The electron density of **1** is shown in yellow, while the inhibitor is illustrated as blue sticks. (**B**) The D-DT-**1** crystal structure (blue) demonstrated high superposition agreement to the corresponding structure of apo D-DT (grey). Binding of **1** does not induce any major conformational changes in the active site environment of D-DT, including the C-terminus. The catalytic residue Pro1 and **1** are shown as blue sticks. (**C**) The inhibitor forms a number of hydrogen bonding and electrostatic interactions with active site residues. The D-DT-**1** hydrogen bonds are shown as black dotted lines and the bond's distance is measured in Å. The three residues participating in electrostatic interactions with the carboxylate groups of **1** are presented as transparent spheres. Hydrophophic interactions play a minor but supporting role in stabilizing D-DT-**1** complex.

Figure 4. Correlation analysis of apo D-DT and D-DT-1. The Cα correlation analyses were obtained from 200 ns MD simulations using the high-resolution crystal structures of apo D-DT

(PDB entry: 1DPT) and D-DT-**1** (PDB entry: 8DBB). Side-by-side examination of the (**A**) apo D-DT and (**B**) D-DT-**1** correlation plots demonstrate that binding of the ligand resulted in reduction of intra- and intersubunit communications. The white circle and boxes, shown vertically, highlight the strong to moderate correlation changes occurring within monomer A (circle) or between monomer A and the other two monomers (boxes), as a consequence of ligand binding. The yellow circle and boxes, shown horizontally, highlight the moderate to low correlation changes occurring within monomer A (circle) or between monomer A and the other two monomers (boxes), as a consequence of ligand binding. (**C**) The strong to moderate correlation changes are also mapped on the structure of D-DT.

Figure 5. Illustration MIF and D-DT active site volumes. PyVOL, a PyMOL plugin, was used to visualize, compare, and calculate the active site volumes of apo MIF (magenta), apo D-DT (grey), and D-DT-**1** (blue). For this analysis, the crystal structures of apo MIF (PDB entry: 3DJH), apo D-DT (PDB entry: 1DPT), and D-DT-**1** (PDB entry: 8DBB) were utilized. The active site volumes are shown as blobs and Pro1 as stick.

Figure 6. Side-by-side comparison of the D-DT and MIF active site pockets. In reference to Pro1, the active site pockets of D-DT (grey) and MIF (magenta) have a perpendicular and parallel orientation, respective. This explains why **1** is able to bind D-DT but not MIF. MIF active site favors binding of compounds that adopt orientations similar to that of ISO-1.

Figure 7. Structural basis of ligand recognition and functional selectivity for MIF and D-DT. A side-by-side comparison of D-DT-**1** (blue) and MIF-ISO-1 (yellow) crystal structures illustrates the structural differences associated with the functional selectivity of **1**. (**A**) Residue 2 plays a key role in orienting the ligand in the active sites of MIF and D-DT. (**B**) Residue 36 has a dual functional role, which includes ligand recognition and stabilization. For D-DT, ligand

recognition is the primary functional role for Arg36, while Tyr36 of MIF serves as stabilizing factor of ISO-1 after ligand binding. (**C**) The hydrophobic amino acids found in the active site of MIF, but not in D-DT, define the topology of the active site pocket, which drastically differs from that of D-DT (**Fig. S7**).

Figure 8. Neutrophil recruitment assay monitoring the D-DT induced activation of CD74. (**A**) Intratracheal installation of LPS free D-DT triggered recruitment of proinflammatory proteins in the bronchoalveolar lavage fluid of mice. In contrast, saline had not a noticeable effect. These findings agree with a previously established mechanism in which it was shown the action of D-DT is associated with activation of macrophage CD74 [43]. The inflammatory effect of D-DT is suppressed when adding **1**, showing that the compound blocks the D-DT-induced activation of CD74. (**B**) Upon activation of macrophage CD74 by D-DT, neutrophils are recruited in the alveolar space. This action is blocked when **1** is added at a concentration range of 10-40 μM. Data were plotted using four replicates and expressed as mean ± SEM.

TABLE LEGENDS

Table 1: Data collection and refinement statistics for D-DT-1

STAR METHODS

Key resources table

REAGENT or RESOURCE	SOURCE	IDENTIFIER
Bacterial and Virus Strains		
BL21 (DE3) E. coli/pET-11b (human WT MIF)	This study	N/A
BL21 (DE3) E. coli/pET-22b (human WT D-DT)	This study	N/A
Chemicals, Peptides, and Recombinant Proteins		
2,5-Pyridinedicarboxcylic acid (>98% purity)	Acros Organics	Cat# 131870050
4-CPPC (99.4% purity)	Axon Medchem	Cat# 3189
4-hydroxyphenylatepyruvate (>95% purity)	TCI	Cat# H0294
4-Phenylpyridine (>98% purity)	TCI	Cat# P0162
Ammonium Acetate (97.0 % purity)	VWR	Cat# BDH9204
Ampicillin Sodium Salt	VWR	Cat# 97061-442
Boric Acid (≥99.5% purity)	VWR	Cat# BDH9222
DMSO (≥99.9% purity)	VWR	Cat# 97061-250
Isopropyl b-D-1-thiogalactopyranoside (IPTG)	Bioland Scientific	Cat# CI01
Luria Broth (LB)	VWR	Cat# 97064-114
Pyridine-2-carboxylic acid (>99% purity)	TCI	Cat# P0421
Nicotinic acid (99.5% purity)	Acros Organics	Cat# 128290050
Terephthalic acid (>99% purity)	TCI	Cat# T0166
Triton X-114 (proteomics grade)	VWR	Cat#M144-1L
WT D-DT	This study	N/A
WT MIF	This study	N/A
Critical Commercial Assays		
Pierce BCA Protein Assay Kit	Thermo-Fisher	Cat# 23225
Hema III Staining Solutions	Thermo-Fischer	Cat# 122911
Deposited Data		
WT MIF	Crichlow et al., 2009	PDB: 3DJH
WT DDT	Sugimoto et al., 1999	PDB: 1DPT
D-DT-1	This Paper	PDB: 8DBB
Recombinant DNA		
pET11b- WT MIF	This study	N/A
pET22b-WT D-DT	This study	N/A
Experimental Models: Cell Lines		
BL21(DE3) Competent Cells	Agilent Technologies	Cat# 200131
Experimental Models: Organisms		
C57BL6/J male mice	Jackson Laboratory	RRID: IMSR_JAX:000664
Software and Algorithms		
Aimless	CCP4	https://www.ccp4.ac.uk/html/aimless.html
CHARMM36 Force Field	University of Maryland School of Pharmacy	http://mackerell.umaryland.edu/charmm_ff.shtml

COOT	MRC Laboratory of Molecular Biology (LMB)	https://www2.mrc-lmb.cam.ac.uk/personal/pemsley/coot/
CHARMM General Force Field (CGenFF)	University of Maryland	https://cgenff.umaryland.edu/
GROMACS	Abraham et al. (2015)	https://www.gromacs.org/index.html
G_Correlation	O. Lange et al. (2005)	https://www.mpinat.mpg.de/grubmueller/g_correlation
MATLAB	MathWorks	https://www.mathworks.com/products/matlab.html
MolGpKa	Xundrug	https://xundrug.cn/molgpka
Molrep	CCP4	https://www.ccp4.ac.uk/html/molrep.html
Nanoanalyze 3.11.0	TA Instruments	https://www.tainstruments.com/
Nanoscale Molecular Dynamics	University of Illinois at Urbana-Champaign	http://www.ks.uiuc.edu/Research/namd/
PRODRG	CCP4	https://www.ccp4.ac.uk/html/cprodrg.html
Prism	Graphpad	https://www.graphpad.com/scientific-software/prism/
PyMOL	DeLano Scientific LLC	http://www.pymol.org/
PyVOL	Smith et al. (2019)	https://schlessinger-lab.github.io/pyvol/index.html
Refmac5	CCP4	https://www.ccp4.ac.uk/html/refmac5/description.html
SUPERPOSE	CCP4	http://www.ccp4.ac.uk/html/superpose.html
Visual Molecular Dynamics	University of Illinois at Urbana-Champaign	http://www.ks.uiuc.edu/Research/vmd/
Origin 2019b	OriginLab	https://www.originlab.com/
XDS	Kabsch (2010)	https://xds.mr.mpg.de/
Other		
Advanced Light Source beamline 8.2.1	Lawrence Livermore National Labs	https://als.lbl.gov/
Circular dichroism spectropolarimeter	Jasco Inc.	Model# J-810
Affinity ITC calorimeter	TA Instruments	Model# Affinity ITC
Microplate reader	TECAN	Model# Infinite M-Plex

RESOURCE AVAILABILITY

Lead contact

Further information and requests for resources and reagents should be directed to and will be fulfilled by the lead contact, Georgios Pantouris (gpantouris@pacific.edu)

Materials availability

This study did not generate new unique reagents.

Data and code availability

- X-ray crystallographic data (D-DT-**1**) have been deposited at wwPDB and are publicly available as of the date of publication. The accession number is listed in the key resources table.
- This paper does not report any original code or algorithm.
- Any additional information required to reanalyze the data reported in this paper is available from the lead contact upon request.

EXPERIMENTAL MODEL AND SUBJECT DETAILS

Cell lines

Recombinant MIF and D-DT proteins were produced and purified from bacterial cells, E. coli strain BL21-(DE3) (Agilent Technologies).

Organisms

Activation of CD74 by D-DT or D-DT-1 complex was evaluated *in vivo* using 10–12 weeks old C57BL6/J male mice (Jackson Laboratory - Bar Harbor, ME). The mice were housed in a pathogen-free animal facility, at Cooper University Hospital, Camden, NJ, USA (IACUC protocol approved by Cooper University Hospital, Camden, NJ, USA).

METHOD DETAILS

Protein Expression and Purification. MIF and D-DT were expressed and purified as previously described [35,51]. Briefly, pET11b and pET22b plasmids expressing MIF and D-DT, respectively, were transformed into BL21 (DE3) competent cells according to the heat shock method. The cells were grown in LB broth enriched with 100 μg/mL ampicillin, at the optimal temperature of 37°C. When the solution's optical density at 600 nm became 0.6-0.8, the cell cultures were induced with 1 mM IPTG for 4 hours at 37°C. Following, the cells were collected by centrifugation, washed with the corresponding MIF or D-DT lysis buffer (20 mM Tris.HCl, 20 mM NaCl, pH 7.4 for MIF and 20 mM Tris.HCl, 20 mM NaCl, pH 8.5 for D-DT), and stored at -80°C. For protein purification, the cells were lysed via sonication, centrifuged to remove cell debris, and filtered with a 0.22 μm PES syringe filter (Bioland Scientific LLC). The MIF lysate was loaded onto a 5 ml Q-Sepharose column connected in series with a second 120 ml Q-Sepharose column. MIF did not bind to either column and eluted in the flow through with a ~95% purity. For D-DT purification, the lysate was loaded onto a 5mL Q-Sepharose column and eluted with 5% of 20 mM Tris.HCl, 1 M NaCl, pH 8.5. The two proteins were further purified by size exclusion chromatography using a 16/60 Superdex 75 column (Cytiva, Marlborough, MA). For this step, the lysis buffers of MIF and D-DT were used as corresponding running buffers. Protein purity and concentration were determined by sodium dodecyl sulfate–polyacrylamide gel electrophoresis (SDS-Page) and bicinchoninic acid (BCA) protein assay, respectively.

Kinetic Experiments. The multipoint kinetic experiments were carried out in a 96-well microplate according to previously published protocols [35,40]. A 30 mM stock solution of 4-HPP was prepared in 0.5 M ammonium acetate pH 6.2 and the keto tautomer was formed after an overnight incubation at room temperature. This stock was used to create a working concentration

gradient of 0 to 2 mM. Compound **1** was prepared in 100% DMSO and used at final concentration ranges of 0-50 μM and 0-3000 μM for D-DT and MIF, respectively. In all experiments, the final concentration of DMSO was 1%. For the MIF assays, EDTA was also added at a final concentration of 1 mM. Borate was added at a final concentration of 0.420 M and the reaction was initiated by adding MIF or D-DT at a final concentration of 50 nM or 250 nM, respectively. The formation of enol-borate complex was monitored at 306 nm (ε_{306} = 11400 M^{-1} cm^{-1}) in a Tecan Infinite M-Plex microplate reader (TECAN). Each experiment was conducted for either 180 seconds (MIF) or 300 seconds (D-DT) and the data was analyzed in GraphPad Prism 9.4.1. For the single point kinetic experiments, 4-HPP and **1**-**5** were used at final concentrations of 1 mM and 100 μM, respectively, while the procedure was similar to what we described above. All kinetic experiments were performed in triplicate.

Isothermal calorimetry. The ITC experiments were carried out in an affinity ITC calorimeter (TA instruments) with all samples being prepared in 20 mM phosphate buffer, pH 6.2 and 1% DMSO and degassed prior to each experiment. For the titration experiment, **1** was deposited into a 264 μL rotating syringe, while D-DT was placed in the isothermal sample cell. D-DT and **1** were tested at a final concentration of 500 μM and 100 μM, respectively. The control run utilized 20 mM phosphate buffer, pH 6.2 and 1% DMSO in the sample cell rather than protein. The contents of the syringe were then injected into the sample cell over 50 steps, each step releasing 3.5 μL. Each injection took place over 4 seconds with a 300-second delay. The syringe speed was set to 125 revolutions per minute (RPM) to ensure proper mixing of the samples. Before the first injection and subsequent data collection, the calorimeter was equilibrated for 1800 s. Data were analyzed using the NanoAnalyze software (version 3.11.0). The heat plot for D-DT-**1** was corrected against the Buffer-**1** heat plot and fitted in the independent model.

Circular dichroism spectroscopy. Thermal denaturation experiments were performed in a Jasco J-810 circular dichroism spectropolarimeter following the protocol described before [52]. D-DT and **1** were prepared in 20 mM Tris.HCl, 20 mM NaCl, pH 7.4 at final concentrations of 20 μM and 0-200 μM, respectively. Before each experiment, all solutions were degassed with ultra-high purity grade nitrogen. The CD spectra of apo D-DT or D-DT-**1** were recorded from 20°C to 90°C at a rate of 0.5°C/min. The fraction of unfolded D-DT over temperature was analyzed in Origin 2019b.

Protein crystallography and data analysis. Crystallization of D-DT-**1** was performed in a 24-well plate (Hampton research) using the hanging drop method. D-DT was concentrated to 12 mg/ml and mixed at 1:1 (v/v) ratio with well solutions containing 24-30% (w/v) PEG 4000, 0.1 M sodium citrate (pH 5.2-6.2), and 0.2 M ammonium sulfate. The triangular shaped crystals of apo D-DT were formed within 1-2 weeks and soaked into equilibrated drops of the mother liquor enriched with 100 mM of **1**. Due to the high concentration of PEG 4000, the crystals were flash frozen without a cryoprotectant. Single wavelength (1.00004 Å) diffraction trials were performed at Lawrence Berkeley National Laboratory using the Advanced Light Source (ALS) beamline 8.2.1. All diffraction trials were performed at 100 K and a complete data set was collected to 1.30 Å. Data reduction, including integration and scaling was accomplished using XDS [53] while final merging was achieved with aimless [54]. The crystal structure of D-DT-**1** was solved by molecular replacement using Molrep, a CCP4-supported program [55]. Apo D-DT (PDB entry: 1DPT) was used as the search structure, producing an initial model in a P3 space group. The model was further refined using Refmac5 [56] and COOT [57] and visualized in PyMOL [58]. Finally, the electron density of **1** was clearly seen in all active sites. The coordinates and crystallographic information files of **1** were generated by PRODRG (CCP4-supported program). Structural

alignment was accomplished using Superpose [55]. The final model has been deposited in worldwide Protein Data Bank with the identification number 8DBB.

Molecular Dynamics Simulations. MD simulations of apo D-DT and D-DT-**1** were performed as previously reported [52]. The models used for the simulations were obtained from the crystal structures of apo D-DT (PDB entry: 1DPT) and D-DT-**1** (PDB entry: 8DBB). Using PyMOL, the protein's biological assembly was generated, and non-protein atoms were removed. A protein structure file (PSF) and PDB pair that included the missing hydrogens was generated utilizing the autoPSF plug-in of Visual Molecular Dynamics (VMD) program [59]. The PSF/PDB pair for D-DT was produced from CHARMM36 forcefield topology [60]. The ionization state of **1** was assigned using MolGpka [61], while its topology file was generated using CHARMM general force field (CGenFF) [62]. Solvated PSF and PDB were produced by the VMD solvate plugin with TIP3P waters. The system was then minimized and heated to 300K in a stepwise fashion. Before initiating the 200 ns run, the system was equilibrated at 300K for 1ns. Generalized cross-correlation analysis of Cα-atoms was performed using g_correlation [63], a GROMACS plug-in [64,65]. RMSF analysis was performed by GROMACS. All simulations were run in triplicate.

Removal of bacterial lipopolysaccharides (LPS). Prior the neutrophil recruitment assay, D-DT was treated for removal of bacterial LPS following a previously established protocol [66]. The procedure was initiated by mixing 30 mL of ice-cold LPS-free phosphate buffered saline (PBS) pH 7.40, with 200 µL D-DT, and 1% Triton X-114 (VWR life science). The mixture of PBS/D-DT/triton X-114 was subsequently incubated at 4°C and 37°C for 30 and 10 minutes, respectively. The first incubation step was performed under gentle mixing while second incubation step was undisrupted. At the end of the 10-minute incubation, the mixture was transferred to eppendorf tubes and centrifuged to form two phases. The lower phase, which

contained triton X-114 and LPS were disposed, while the upper phase (D-DT) was used for two additional rounds of purification. At the end of the third purification, D-DT was dialyzed for 16 hours in a 4 L LPS-free PBS (pH 7.40) solution. The next day, protein concentration was determined by the BCA assay and D-DT aliquots were stored in -80ºC.

Neutrophil recruitment assay. Wild-type male mice (10–12 weeks old) of C57BL6/J genetic background were purchased from Jackson Laboratory (Bar Harbor, ME) and housed in a pathogen-free animal facility, at Cooper University Hospital, Camden, NJ, USA. Mice were administered a one-time intratracheal instillation of 50 µl PBS (vehicle) with or without LPS-free D-DT and/or **1**. The final concentration of D-DT and **1** was 20 µg/ml and 0-40 µM, respectively. Intratracheal instillation was performed following the methodology previously described [44] with some modifications. Six hours after the administration of experimental solutions, the mice were sacrificed to collect BAL fluid. The total protein content in the BAL fluid was measured by BCA assay. Approximately 1ml of the BAL fluid was pelleted by centrifugation at 1000 rpm for 10 min at 4°C. Following, the cell pellet was resuspended in 200 µl 1x PBS and centrifugation was repeated one more time at room temperature. The slides were air dried and stained with Hema III Differential Quick Stain. Neutrophils were counted manually in the smears to calculate their total percentage. Briefly, the cytosmear was randomly divided into 4-5 arbitrary areas that housed the maximum number of neutrophils. Two hundred different inflammatory cell types, including neutrophils, were counted in these areas from which the percentage of neutrophils was calculated. At least 4 mice were used for each experimental group. The animal study protocol was approved by the Institutional Animal Care and Use Committee (IACUC) of Cooper University Hospital, Camden, NJ, USA. Statistical analysis was done with GraphPad Prism 9.4.1 by one-way ANOVA with Tukey's post-hoc correction.

QUANTIFICATION AND STATISTICAL ANALYSIS

All single point and kinetic experiments were carried out in triplicate (n=3) with the data being analyzed in ORIGIN 2019b. For both **Figures 1** and **2**, the error is represented as standard deviation. The D-DT-**1** crystal structure was refined using the R_{free} value along with a Ramachandran plot to fix angle outliers before submission to PDB/RCSB (https://www.rcsb.org). All statistics for the structure are present in **Table 1** and the "Full wwPDB X-ray Structure Validation Report", which contains a variety of structure metrics, is available in the RCSB database. All MD data was obtained in triplicate (n=3), root mean square fluctuation (RMSF) was averaged, presented with an error value obtained from the standard deviation, and plotted (**Figure S5**) using ORIGIN 2019b. In vivo studies utilizing mice had a minimum group size of 4 (n=4), the data was analyzed using GraphPad Prism 9.4.1 by one-way ANOVA with Tukey's post-hoc correction. The data is presented in **Figure 8** as the mean with standard error of the mean (SEM).

REFERENCES

1. Merk, M., Zierow, S., Leng, L., Das, R., Du, X., Schulte, W., Fan, J., Lue, H., Chen, Y., Xiong, H., et al. (2011). The D-dopachrome tautomerase (DDT) gene product is a cytokine and functional homolog of macrophage migration inhibitory factor (MIF). Proc Natl Acad Sci U S A *108*, E577-585. 10.1073/pnas.1102941108.
2. Leng, L., Metz, C.N., Fang, Y., Xu, J., Donnelly, S., Baugh, J., Delohery, T., Chen, Y., Mitchell, R.A., and Bucala, R. (2003). MIF signal transduction initiated by binding to CD74. J Exp Med *197*, 1467-1476. 10.1084/jem.20030286.
3. Rosengren, E., Bucala, R., Aman, P., Jacobsson, L., Odh, G., Metz, C.N., and Rorsman, H. (1996). The immunoregulatory mediator macrophage migration inhibitory factor (MIF) catalyzes a tautomerization reaction. Mol Med *2*, 143-149.
4. Nishihira, J., Fujinaga, M., Kuriyama, T., Suzuki, M., Sugimoto, H., Nakagawa, A., Tanaka, I., and Sakai, M. (1998). Molecular cloning of human D-dopachrome tautomerase cDNA: N-terminal proline is essential for enzyme activation. Biochem Biophys Res Commun *243*, 538-544. 10.1006/bbrc.1998.8123.
5. Xiao, Z., Chen, D., Mulder, F., Song, S., van der Wouden, P.E., Cool, R.H., Melgert, B.N., Poelarends, G.J., and Dekker, F.J. (2022). 4-Iodopyrimidine Labeling Reveals Nuclear Translocation and Nuclease Activity for Both MIF and MIF2. Chemistry *28*, e202103030. 10.1002/chem.202103030.
6. Wang, Y., An, R., Umanah, G.K., Park, H., Nambiar, K., Eacker, S.M., Kim, B., Bao, L., Harraz, M.M., Chang, C., et al. (2016). A nuclease that mediates cell death induced by DNA damage and poly(ADP-ribose) polymerase-1. Science *354*. 10.1126/science.aad6872.
7. Bloom, B.R., and Bennett, B. (1966). Mechanism of a reaction in vitro associated with delayed-type hypersensitivity. Science *153*, 80-82. 10.1126/science.153.3731.80.
8. Calandra, T., and Roger, T. (2003). Macrophage migration inhibitory factor: a regulator of innate immunity. Nat Rev Immunol *3*, 791-800. 10.1038/nri1200.
9. Shi, X., Leng, L., Wang, T., Wang, W., Du, X., Li, J., McDonald, C., Chen, Z., Murphy, J.W., Lolis, E., et al. (2006). CD44 is the signaling component of the macrophage migration inhibitory factor-CD74 receptor complex. Immunity *25*, 595-606. 10.1016/j.immuni.2006.08.020.
10. Bernhagen, J., Krohn, R., Lue, H., Gregory, J.L., Zernecke, A., Koenen, R.R., Dewor, M., Georgiev, I., Schober, A., Leng, L., et al. (2007). MIF is a noncognate ligand of CXC chemokine receptors in inflammatory and atherogenic cell recruitment. Nat Med *13*, 587-596. 10.1038/nm1567.
11. Alampour-Rajabi, S., El Bounkari, O., Rot, A., Müller-Newen, G., Bachelerie, F., Gawaz, M., Weber, C., Schober, A., and Bernhagen, J. (2015). MIF interacts with CXCR7 to promote receptor internalization, ERK1/2 and ZAP-70 signaling, and lymphocyte chemotaxis. FASEB J *29*, 4497-4511. 10.1096/fj.15-273904.
12. Schwartz, V., Lue, H., Kraemer, S., Korbiel, J., Krohn, R., Ohl, K., Bucala, R., Weber, C., and Bernhagen, J. (2009). A functional heteromeric MIF receptor formed by CD74 and CXCR4. FEBS Lett *583*, 2749-2757. 10.1016/j.febslet.2009.07.058.
13. Tilstam, P.V., Schulte, W., Holowka, T., Kim, B.S., Nouws, J., Sauler, M., Piecychna, M., Pantouris, G., Lolis, E., Leng, L., et al. (2021). MIF but not MIF-2 recruits inflammatory macrophages in an experimental polymicrobial sepsis model. J Clin Invest *131*. 10.1172/jci127171.
14. Yang, S., He, P., Wang, J., Schetter, A., Tang, W., Funamizu, N., Yanaga, K., Uwagawa, T., Satoskar, A.R., Gaedcke, J., et al. (2016). A Novel MIF Signaling Pathway Drives the Malignant Character of Pancreatic Cancer by Targeting NR3C2. Cancer Res *76*, 3838-3850. 10.1158/0008-5472.Can-15-2841.

15. Baugh, J.A., Chitnis, S., Donnelly, S.C., Monteiro, J., Lin, X., Plant, B.J., Wolfe, F., Gregersen, P.K., and Bucala, R. (2002). A functional promoter polymorphism in the macrophage migration inhibitory factor (MIF) gene associated with disease severity in rheumatoid arthritis. Genes Immun *3*, 170-176. 10.1038/sj.gene.6363867.
16. Thiele, M., Kerschbaumer, R.J., Tam, F.W.K., Völkel, D., Douillard, P., Schinagl, A., Kühnel, H., Smith, J., McDaid, J.P., Bhangal, G., et al. (2015). Selective Targeting of a Disease-Related Conformational Isoform of Macrophage Migration Inhibitory Factor Ameliorates Inflammatory Conditions. The Journal of Immunology *195*, 2343-2352. 10.4049/jimmunol.1500572.
17. Schinagl, A., Thiele, M., Douillard, P., Völkel, D., Kenner, L., Kazemi, Z., Freissmuth, M., Scheiflinger, F., and Kerschbaumer, R.J. (2016). Oxidized macrophage migration inhibitory factor is a potential new tissue marker and drug target in cancer. Oncotarget *7*, 73486-73496. 10.18632/oncotarget.11970.
18. Skeens, E., Gadzuk-Shea, M., Shah, D., Bhandari, V., Schweppe, D.K., Berlow, R.B., and Lisi, G.P. (2022). Redox-dependent structure and dynamics of macrophage migration inhibitory factor reveal sites of latent allostery. Structure *30*, 840-850 e846. 10.1016/j.str.2022.03.007.
19. Sun, H.W., Bernhagen, J., Bucala, R., and Lolis, E. (1996). Crystal structure at 2.6-A resolution of human macrophage migration inhibitory factor. Proc Natl Acad Sci U S A *93*, 5191-5196. 10.1073/pnas.93.11.5191.
20. Lubetsky, J.B., Dios, A., Han, J., Aljabari, B., Ruzsicska, B., Mitchell, R., Lolis, E., and Al-Abed, Y. (2002). The tautomerase active site of macrophage migration inhibitory factor is a potential target for discovery of novel anti-inflammatory agents. J Biol Chem *277*, 24976-24982. 10.1074/jbc.M203220200.
21. Cho, Y., Crichlow, G.V., Vermeire, J.J., Leng, L., Du, X., Hodsdon, M.E., Bucala, R., Cappello, M., Gross, M., Gaeta, F., et al. (2010). Allosteric inhibition of macrophage migration inhibitory factor revealed by ibudilast. Proc Natl Acad Sci U S A *107*, 11313-11318. 10.1073/pnas.1002716107.
22. Pantouris, G., Syed, M.A., Fan, C., Rajasekaran, D., Cho, T.Y., Rosenberg, E.M., Jr., Bucala, R., Bhandari, V., and Lolis, E.J. (2015). An Analysis of MIF Structural Features that Control Functional Activation of CD74. Chem Biol *22*, 1197-1205. 10.1016/j.chembiol.2015.08.006.
23. Rajasekaran, D., Zierow, S., Syed, M., Bucala, R., Bhandari, V., and Lolis, E.J. (2014). Targeting distinct tautomerase sites of D-DT and MIF with a single molecule for inhibition of neutrophil lung recruitment. FASEB J *28*, 4961-4971. 10.1096/fj.14-256636.
24. Sugimoto, H., Taniguchi, M., Nakagawa, A., Tanaka, I., Suzuki, M., and Nishihira, J. (1999). Crystal structure of human D-dopachrome tautomerase, a homologue of macrophage migration inhibitory factor, at 1.54 A resolution. Biochemistry *38*, 3268-3279. 10.1021/bi982184o.
25. Merk, M., Mitchell, R.A., Endres, S., and Bucala, R. (2012). D-dopachrome tautomerase (D-DT or MIF-2): doubling the MIF cytokine family. Cytokine *59*, 10-17. 10.1016/j.cyto.2012.03.014.
26. Zan, C., Yang, B., Brandhofer, M., El Bounkari, O., and Bernhagen, J. (2022). D-dopachrome tautomerase in cardiovascular and inflammatory diseases-A new kid on the block or just another MIF? FASEB J *36*, e22601. 10.1096/fj.202201213R.
27. Guo, D., Guo, J., Yao, J., Jiang, K., Hu, J., Wang, B., Liu, H., Lin, L., Sun, W., and Jiang, X. (2016). D-dopachrome tautomerase is over-expressed in pancreatic ductal adenocarcinoma and acts cooperatively with macrophage migration inhibitory factor to promote cancer growth. Int J Cancer *139*, 2056-2067. 10.1002/ijc.30278.
28. Song, S., Liu, B., Habibie, H., van den Bor, J., Smit, M.J., Gosens, R., Wu, X., Brandsma, C.A., Cool, R.H., Haisma, H.J., et al. (2021). D-dopachrome tautomerase contributes to lung epithelial repair via atypical chemokine receptor 3-dependent Akt signaling. EBioMedicine *68*, 103412. 10.1016/j.ebiom.2021.103412.

29. Miller, E.J., Li, J., Leng, L., McDonald, C., Atsumi, T., Bucala, R., and Young, L.H. (2008). Macrophage migration inhibitory factor stimulates AMP-activated protein kinase in the ischaemic heart. Nature *451*, 578-582. 10.1038/nature06504.
30. Qi, D., Atsina, K., Qu, L., Hu, X., Wu, X., Xu, B., Piecychna, M., Leng, L., Fingerle-Rowson, G., Zhang, J., et al. (2014). The vestigial enzyme D-dopachrome tautomerase protects the heart against ischemic injury. J Clin Invest *124*, 3540-3550. 10.1172/jci73061.
31. Kim, B.S., Tilstam, P.V., Arnke, K., Leng, L., Ruhl, T., Piecychna, M., Schulte, W., Sauler, M., Frueh, F.S., Storti, G., et al. (2020). Differential regulation of macrophage activation by the MIF cytokine superfamily members MIF and MIF-2 in adipose tissue during endotoxemia. FASEB J *34*, 4219-4233. 10.1096/fj.201901511R.
32. Vincent, F.B., Lin, E., Sahhar, J., Ngian, G.S., Kandane-Rathnayake, R., Mende, R., Hoi, A.Y., Morand, E.F., Lang, T., and Harris, J. (2018). Analysis of serum macrophage migration inhibitory factor and D-dopachrome tautomerase in systemic sclerosis. Clin Transl Immunology *7*, e1042. 10.1002/cti2.1042.
33. Tilstam, P.V., Pantouris, G., Corman, M., Andreoli, M., Mahboubi, K., Davis, G., Du, X., Leng, L., Lolis, E., and Bucala, R. (2019). A selective small-molecule inhibitor of macrophage migration inhibitory factor-2 (MIF-2), a MIF cytokine superfamily member, inhibits MIF-2 biological activity. J Biol Chem *294*, 18522-18531. 10.1074/jbc.RA119.009860.
34. Xiao, Z., Osipyan, A., Song, S., Chen, D., Schut, R.A., van Merkerk, R., van der Wouden, P.E., Cool, R.H., Quax, W.J., Melgert, B.N., et al. (2022). Thieno[2,3-d]pyrimidine-2,4(1H,3H)-dione Derivative Inhibits d-Dopachrome Tautomerase Activity and Suppresses the Proliferation of Non-Small Cell Lung Cancer Cells. J Med Chem *65*, 2059-2077. 10.1021/acs.jmedchem.1c01598.
35. Pantouris, G., Bucala, R., and Lolis, E.J. (2018). Structural plasticity in the C-terminal region of macrophage migration inhibitory factor-2 is associated with an induced fit mechanism for a selective inhibitor. Biochemistry *57*, 3599-3605.
36. Norkus, E., Gaidamauskas, E., Stalnioniene, I., and Crans, D.C. (2005). Interaction of pyridine-2,5-dicarboxylic acid with heavy metal ions in aqueous solutions. Heteroatom Chemistry *16*, 285-291. 10.1002/hc.20123.
37. Smith, R.H.B., Dar, A.C., and Schlessinger, A. (2019). PyVOL: a PyMOL plugin for visualization, comparison, and volume calculation of drug-binding sites. bioRxiv, 816702. 10.1101/816702.
38. Al-Abed, Y., and VanPatten, S. (2011). MIF as a disease target: ISO-1 as a proof-of-concept therapeutic. Future Med Chem *3*, 45-63. 10.4155/fmc.10.281.
39. Crichlow, G.V., Lubetsky, J.B., Leng, L., Bucala, R., and Lolis, E.J. (2009). Structural and kinetic analyses of macrophage migration inhibitory factor active site interactions. Biochemistry *48*, 132-139. 10.1021/bi8014423.
40. Pantouris, G., Khurana, L., Ma, A., Skeens, E., Reiss, K., Batista, V.S., Lisi, G.P., and Lolis, E.J. (2020). Regulation of MIF Enzymatic Activity by an Allosteric Site at the Central Solvent Channel. Cell Chem Biol *27*, 740-750 e745. 10.1016/j.chembiol.2020.05.001.
41. Orita, M., Yamamoto, S., Katayama, N., Aoki, M., Takayama, K., Yamagiwa, Y., Seki, N., Suzuki, H., Kurihara, H., Sakashita, H., et al. (2001). Coumarin and chromen-4-one analogues as tautomerase inhibitors of macrophage migration inhibitory factor: discovery and X-ray crystallography. J Med Chem *44*, 540-547. 10.1021/jm000386o.
42. Jasanoff, A., Wagner, G., and Wiley, D.C. (1998). Structure of a trimeric domain of the MHC class II-associated chaperonin and targeting protein Ii. EMBO J *17*, 6812-6818. 10.1093/emboj/17.23.6812.
43. Takahashi, K., Koga, K., Linge, H.M., Zhang, Y., Lin, X., Metz, C.N., Al-Abed, Y., Ojamaa, K., and Miller, E.J. (2009). Macrophage CD74 contributes to MIF-induced pulmonary inflammation. Respir Res *10*, 33. 10.1186/1465-9921-10-33.

44. Pantouris, G., Ho, J., Shah, D., Syed, M.A., Leng, L., Bhandari, V., Bucala, R., Batista, V.S., Loria, J.P., and Lolis, E.J. (2018). Nanosecond Dynamics Regulate the MIF-Induced Activity of CD74. Angew Chem Int Ed Engl *57*, 7116-7119. 10.1002/anie.201803191.
45. Singh, A.K., Pantouris, G., Borosch, S., Rojanasthien, S., and Cho, T.Y. (2017). Structural basis for decreased induction of class IB PI3-kinases expression by MIF inhibitors. J Cell Mol Med *21*, 142-153. 10.1111/jcmm.12949.
46. Skeens, E., Pantouris, G., Shah, D., Manjula, R., Ombrello, M.J., Maluf, N.K., Bhandari, V., Lisi, G.P., and Lolis, E.J. (2022). A Cysteine Variant at an Allosteric Site Alters MIF Dynamics and Biological Function in Homo- and Heterotrimeric Assemblies. Front Mol Biosci *9*, 783669. 10.3389/fmolb.2022.783669.
47. Chen, E., Reiss, K., Shah, D., Manjula, R., Allen, B., Murphy, E.L., Murphy, J.W., Batista, V.S., Bhandari, V., Lolis, E.J., and Lisi, G.P. (2021). A structurally preserved allosteric site in the MIF superfamily affects enzymatic activity and CD74 activation in D-dopachrome tautomerase. J Biol Chem *297*, 101061. 10.1016/j.jbc.2021.101061.
48. Eynde, B.J.V.d., Baren, N.v., and Baurain, J.-F. (2020). Is There a Clinical Future for IDO1 Inhibitors After the Failure of Epacadostat in Melanoma? Annual Review of Cancer Biology *4*, 241-256. 10.1146/annurev-cancerbio-030419-033635.
49. Pantouris, G., Serys, M., Yuasa, H.J., Ball, H.J., and Mowat, C.G. (2014). Human indoleamine 2,3-dioxygenase-2 has substrate specificity and inhibition characteristics distinct from those of indoleamine 2,3-dioxygenase-1. Amino Acids *46*, 2155-2163. 10.1007/s00726-014-1766-3.
50. Edwards, C.J., Feldman, J.L., Beech, J., Shields, K.M., Stover, J.A., Trepicchio, W.L., Larsen, G., Foxwell, B.M., Brennan, F.M., Feldmann, M., and Pittman, D.D. (2007). Molecular profile of peripheral blood mononuclear cells from patients with rheumatoid arthritis. Mol Med *13*, 40-58. 10.2119/2006-000056.Edwards.
51. Khurana, L., ElGindi, M., Tilstam, P.V., and Pantouris, G. (2019). Elucidating the role of an immunomodulatory protein in cancer: From protein expression to functional characterization. Methods Enzymol *629*, 307-360. 10.1016/bs.mie.2019.05.053.
52. Parkins, A., Skeens, E., McCallum, C.M., Lisi, G.P., and Pantouris, G. (2021). The N-terminus of MIF regulates the dynamic profile of residues involved in CD74 activation. Biophys J *120*, 3893-3900. 10.1016/j.bpj.2021.08.025.
53. Kabsch, W. (2010). XDS. Acta Crystallogr D Biol Crystallogr *66*, 125-132. 10.1107/s0907444909047337.
54. Evans, P.R., and Murshudov, G.N. (2013). How good are my data and what is the resolution? Acta Crystallogr D Biol Crystallogr *69*, 1204-1214. 10.1107/s0907444913000061.
55. Winn, M.D., Ballard, C.C., Cowtan, K.D., Dodson, E.J., Emsley, P., Evans, P.R., Keegan, R.M., Krissinel, E.B., Leslie, A.G., McCoy, A., et al. (2011). Overview of the CCP4 suite and current developments. Acta Crystallogr D Biol Crystallogr *67*, 235-242. 10.1107/s0907444910045749.
56. Murshudov, G.N., Skubák, P., Lebedev, A.A., Pannu, N.S., Steiner, R.A., Nicholls, R.A., Winn, M.D., Long, F., and Vagin, A.A. (2011). REFMAC5 for the refinement of macromolecular crystal structures. Acta Crystallogr D Biol Crystallogr *67*, 355-367. 10.1107/s0907444911001314.
57. Emsley, P., and Cowtan, K. (2004). Coot: model-building tools for molecular graphics. Acta Crystallogr D Biol Crystallogr *60*, 2126-2132. 10.1107/s0907444904019158.
58. DeLano, W.L. (2002). The PyMOL Molecular Graphics System. Delano Scientific, San Carlos.
59. Humphrey, W., Dalke, A., and Schulten, K. (1996). VMD: visual molecular dynamics. J Mol Graph *14*, 33-38, 27-38. 10.1016/0263-7855(96)00018-5.
60. Huang, J., Rauscher, S., Nawrocki, G., Ran, T., Feig, M., de Groot, B.L., Grubmüller, H., and MacKerell, A.D., Jr. (2017). CHARMM36m: an improved force field for folded and intrinsically disordered proteins. Nat Methods *14*, 71-73. 10.1038/nmeth.4067.

61. Pan, X., Wang, H., Li, C., Zhang, J.Z.H., and Ji, C. (2021). MolGpka: A Web Server for Small Molecule pKa Prediction Using a Graph-Convolutional Neural Network. Journal of Chemical Information and Modeling *61*, 3159-3165. 10.1021/acs.jcim.1c00075.
62. Vanommeslaeghe, K., Hatcher, E., Acharya, C., Kundu, S., Zhong, S., Shim, J., Darian, E., Guvench, O., Lopes, P., Vorobyov, I., and Mackerell, A.D., Jr. (2010). CHARMM general force field: A force field for drug-like molecules compatible with the CHARMM all-atom additive biological force fields. J Comput Chem *31*, 671-690. 10.1002/jcc.21367.
63. Lange, O.F., and Grubmüller, H. (2006). Generalized correlation for biomolecular dynamics. Proteins *62*, 1053-1061. 10.1002/prot.20784.
64. Van Der Spoel, D., Lindahl, E., Hess, B., Groenhof, G., Mark, A.E., and Berendsen, H.J. (2005). GROMACS: fast, flexible, and free. J Comput Chem *26*, 1701-1718. 10.1002/jcc.20291.
65. Abraham, M.J., Murtola, T., Schulz, R., Páll, S., Smith, J.C., Hess, B., and Lindahl, E. (2015). GROMACS: High performance molecular simulations through multi-level parallelism from laptops to supercomputers. SoftwareX *1-2*, 19-25. https://doi.org/10.1016/j.softx.2015.06.001.
66. Aida, Y., and Pabst, M.J. (1990). Removal of endotoxin from protein solutions by phase separation using Triton X-114. J Immunol Methods *132*, 191-195. 10.1016/0022-1759(90)90029-u.

A

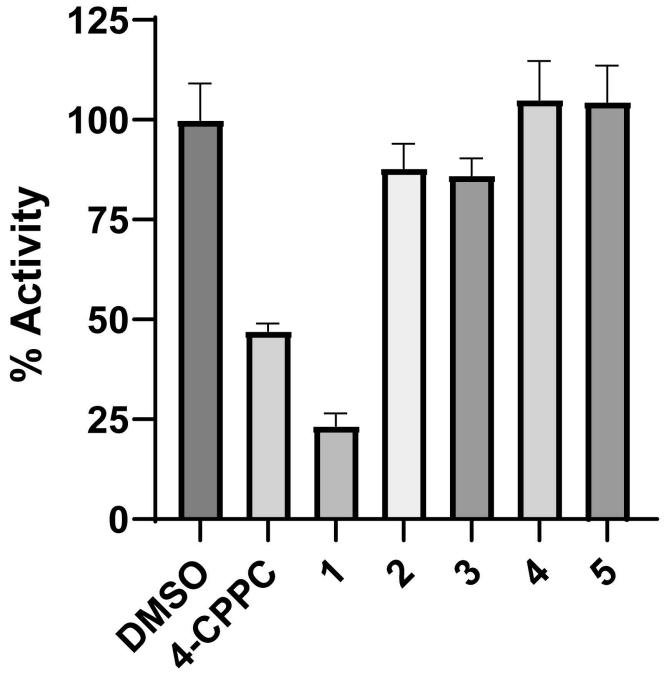

B

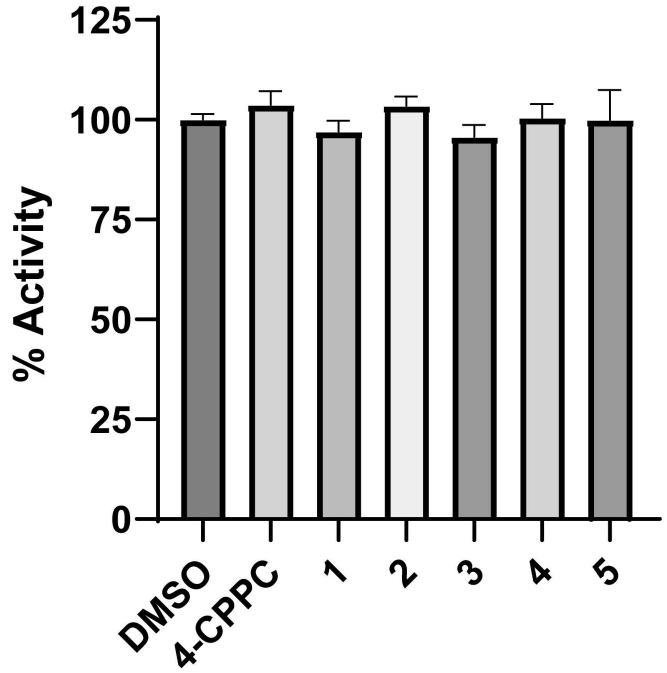

C

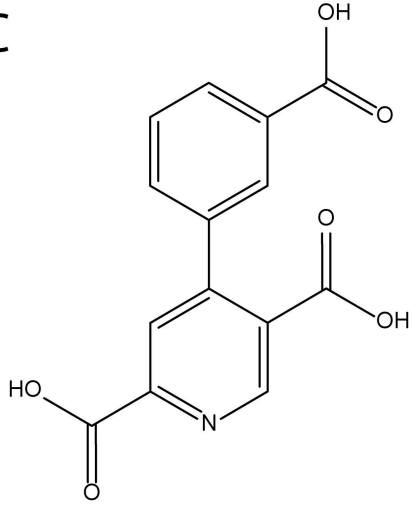

4-CPPC

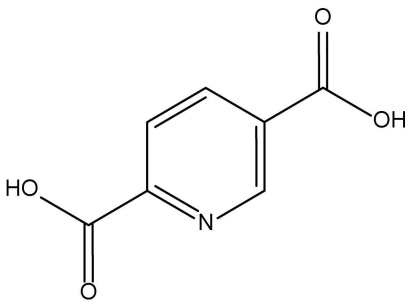

1

2,5-Pyridinedicarboxylic acid

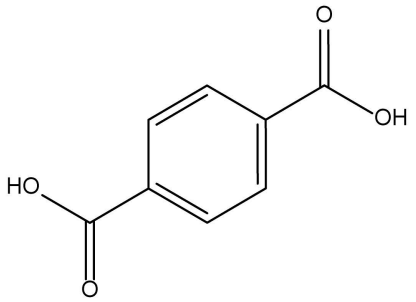

2

Terephthalic acid

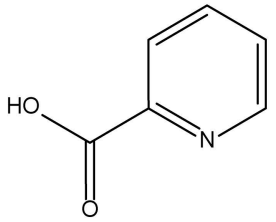

3

Pyridine-2-carboxylic acid

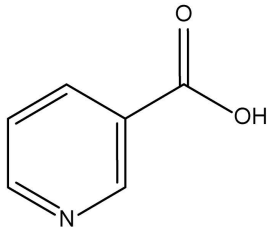

4

Nicotinic acid

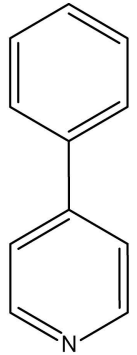

5

4-Phenylpyridine

D-DT

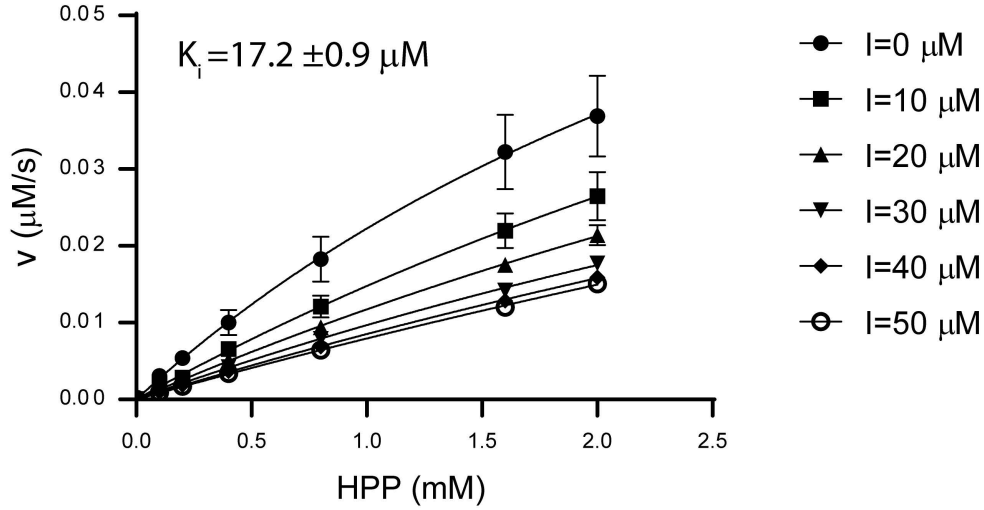
Michaelis-Menten plot
K_i =17.2 ±0.9 μM
v (μM/s)
HPP (mM)
I=0 μM
I=10 μM
I=20 μM
I=30 μM
I=40 μM
I=50 μM

Lineweaver-Burk plot
1/v
1/HPP
I=0 μM
I=10 μM
I=20 μM
I=30 μM
I=40 μM
I=50 μM

Dixon plot
1/v
I (μM)
HPP=0.1 mM
HPP=0.2 mM
HPP=0.4 mM
HPP=0.8 mM
HPP=1.6 mM
HPP=2.0 mM

MIF

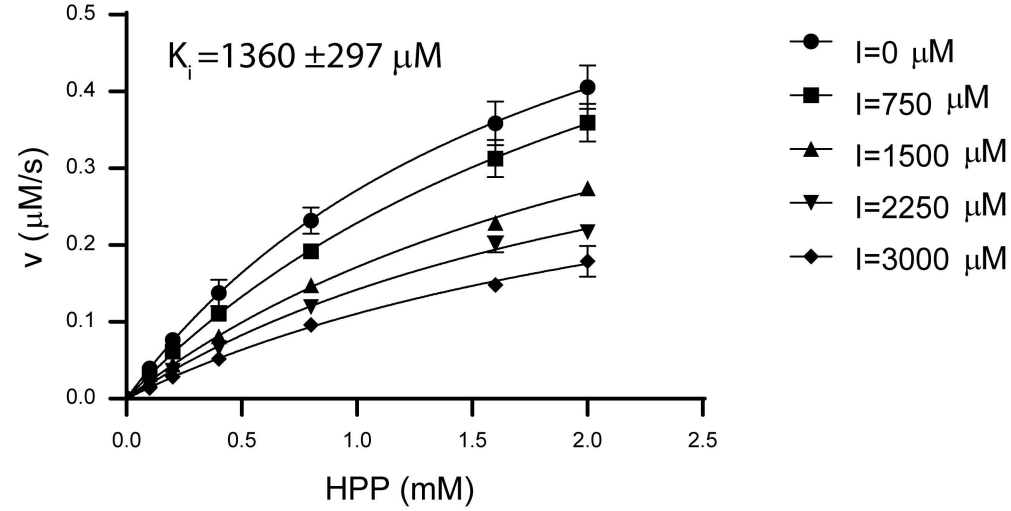
K_i =1360 ±297 μM
v (μM/s)
HPP (mM)
I=0 μM
I=750 μM
I=1500 μM
I=2250 μM
I=3000 μM

1/v
1/HPP
I=0 μM
I=750 μM
I=1500 μM
I=2250 μM
I=3000 μM

1/v
I (μM)
HPP=0.1 mM
HPP=0.2 mM
HPP=0.4 mM
HPP=0.8 mM
HPP=1.6 mM
HPP=2.0 mM

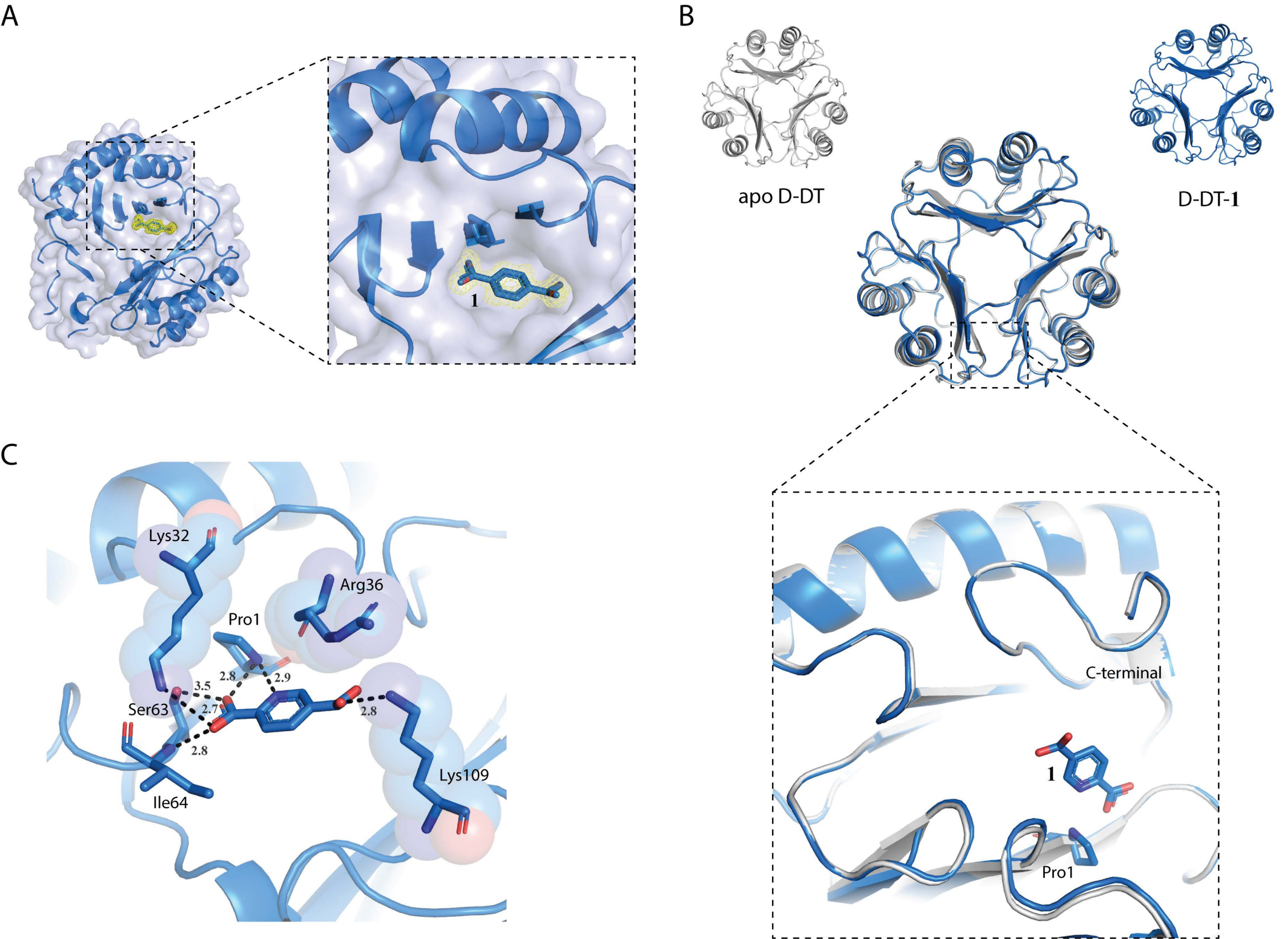
A
1
B
apo D-DT
D-DT-1
C-terminal
1
Pro1
C
Lys32
Arg36
Pro1
2.8
2.9
3.5
2.7
Ser63
2.8
2.8
Lys109
Ile64

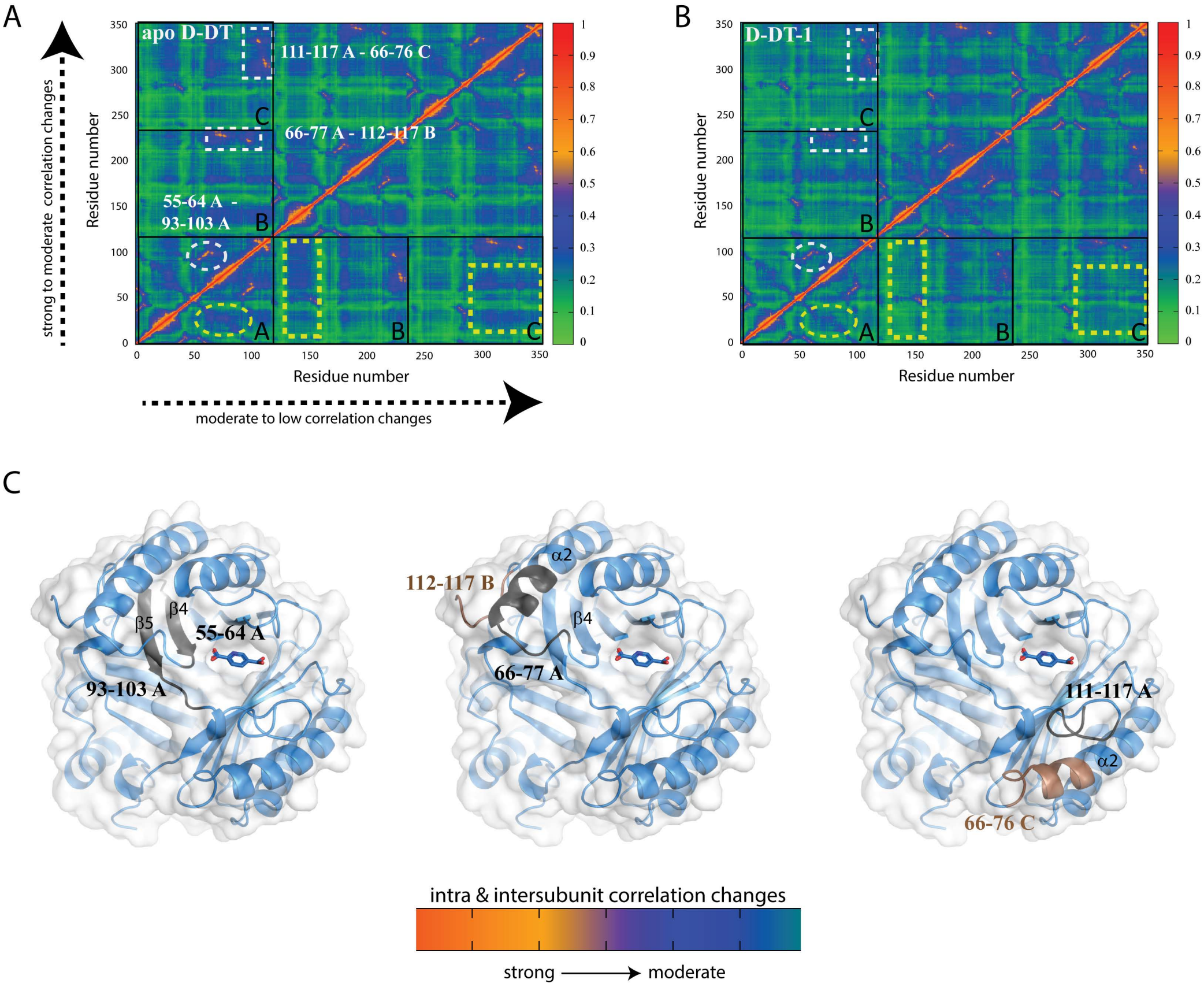
A
apo D-DT
111-117 A - 66-76 C
66-77 A - 112-117 B
55-64 A -
93-103 A
A
B
C
Residue number
Residue number
strong to moderate correlation changes
moderate to low correlation changes
B
D-DT-1
C
A
B
C
Residue number
Residue number
C
β4
β5
55-64 A
93-103 A
α2
112-117 B
β4
66-77 A
111-117 A
α2
66-76 C
intra & intersubunit correlation changes
strong
moderate

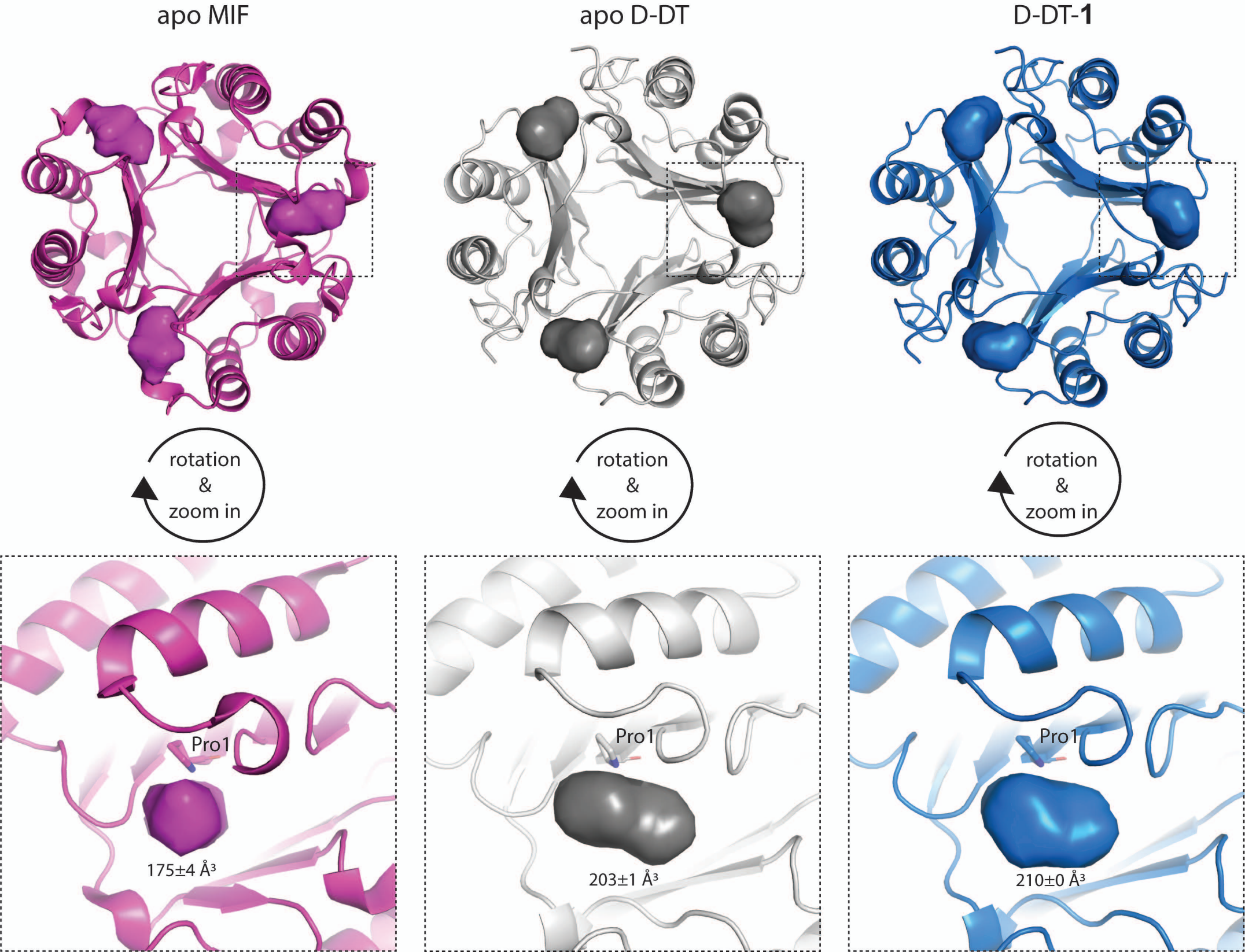
apo MIF
apo D-DT
D-DT-1
rotation & zoom in
rotation & zoom in
rotation & zoom in
Pro1
175±4 Å³
Pro1
203±1 Å³
Pro1
210±0 Å³

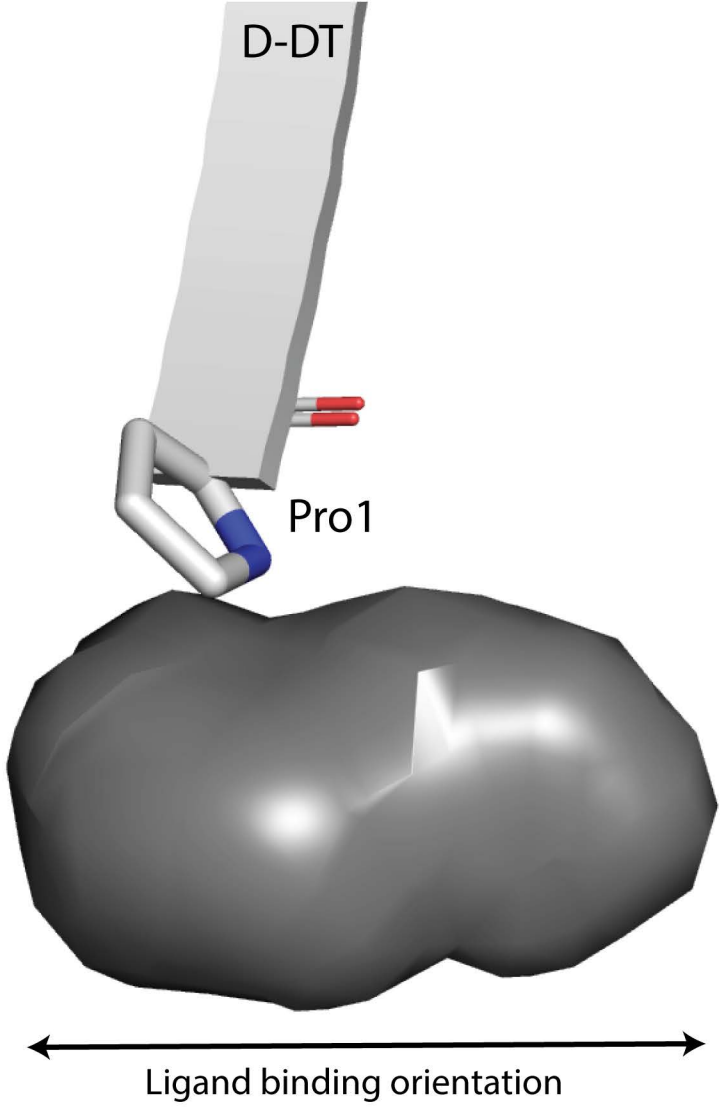
D-DT
Pro1
Ligand binding orientation

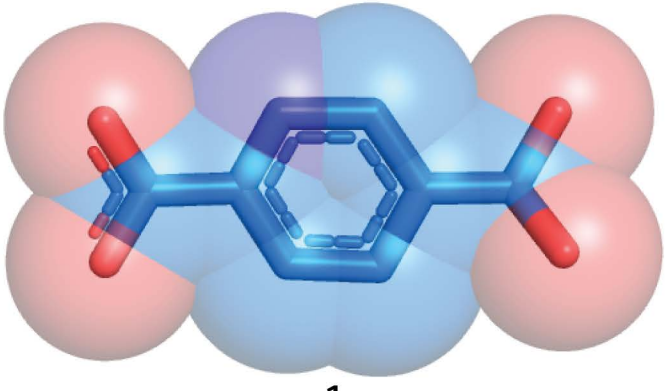
1

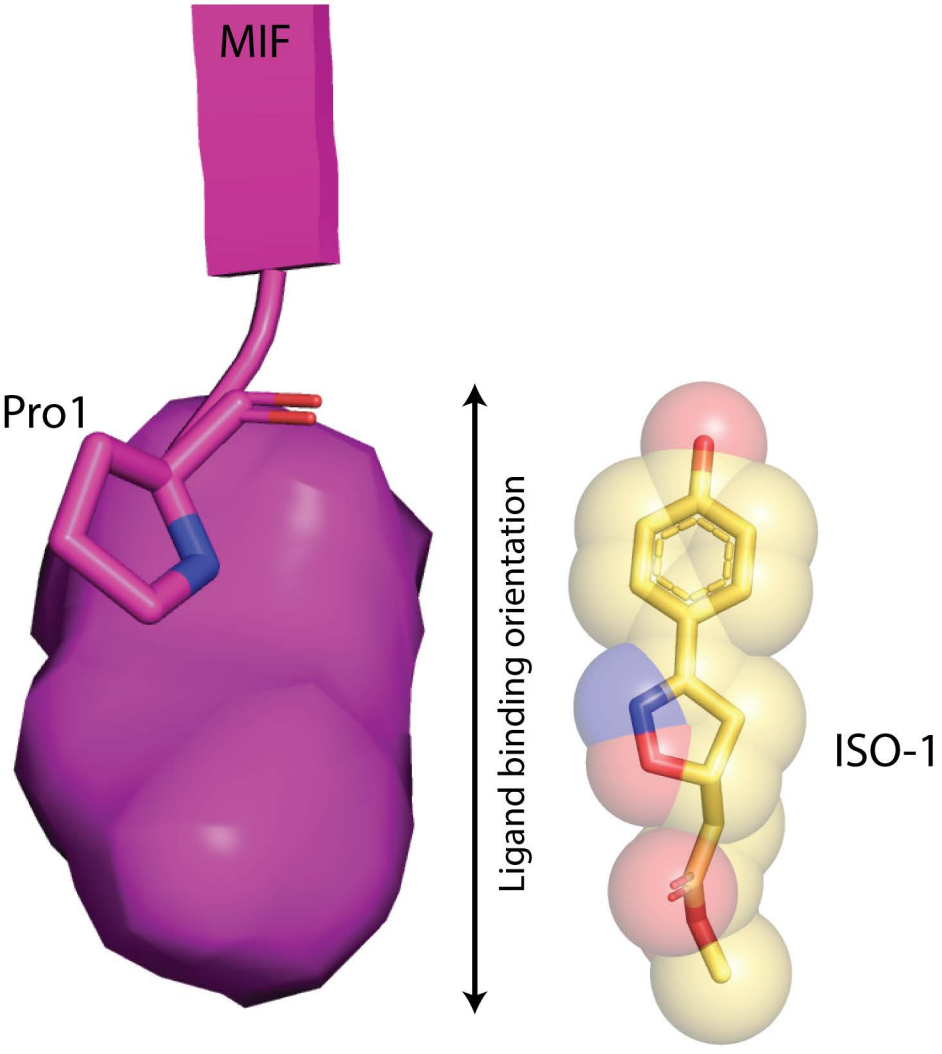
MIF
Pro1
Ligand binding orientation
ISO-1

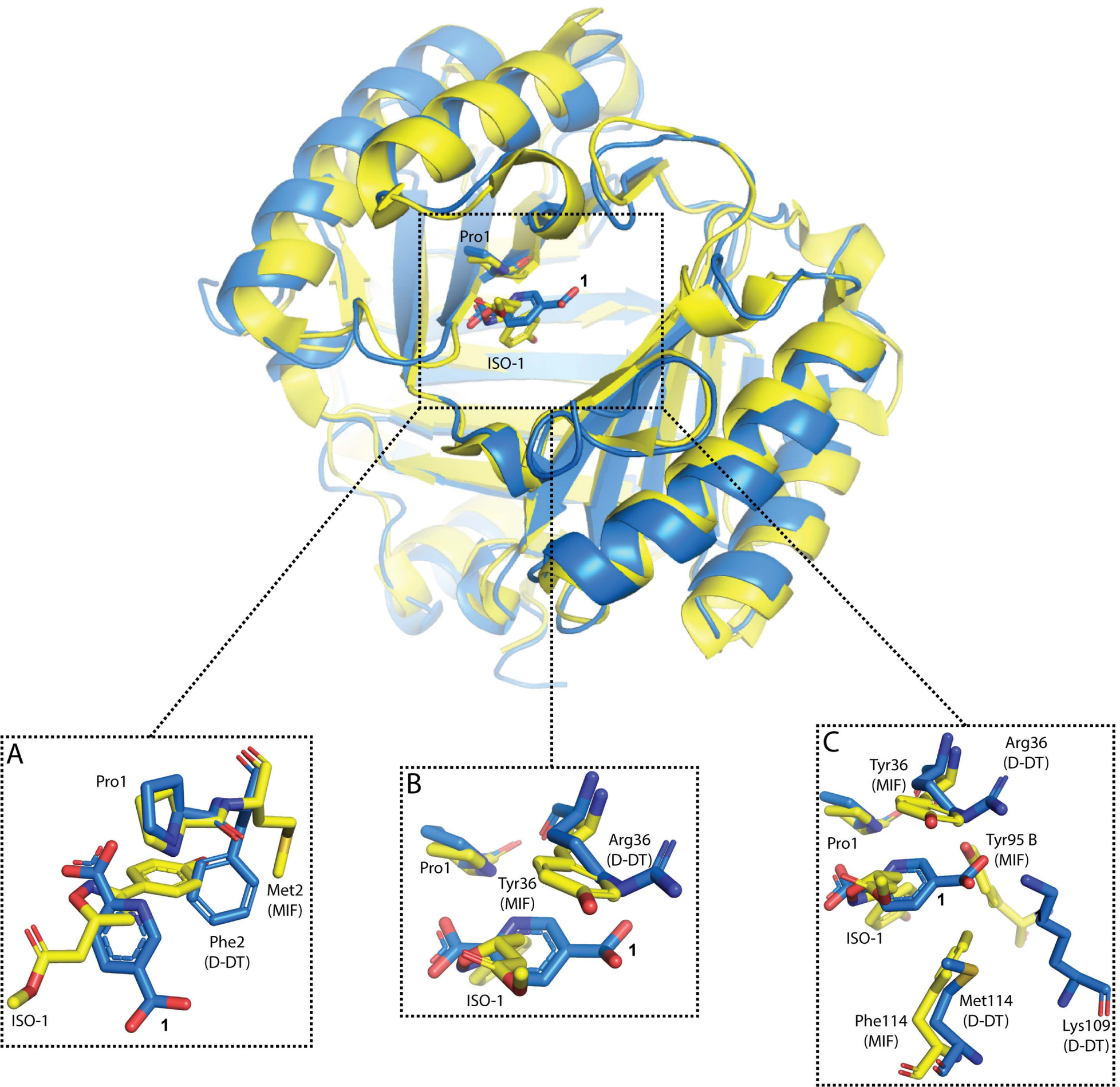
Pro1
1
ISO-1
A
Pro1
Met2
(MIF)
Phe2
(D-DT)
ISO-1
1
B
Pro1
Arg36
(D-DT)
Tyr36
(MIF)
1
ISO-1
C
Tyr36
(MIF)
Arg36
(D-DT)
Pro1
Tyr95 B
(MIF)
1
ISO-1
Met114
(D-DT)
Phe114
(MIF)
Lys109
(D-DT)

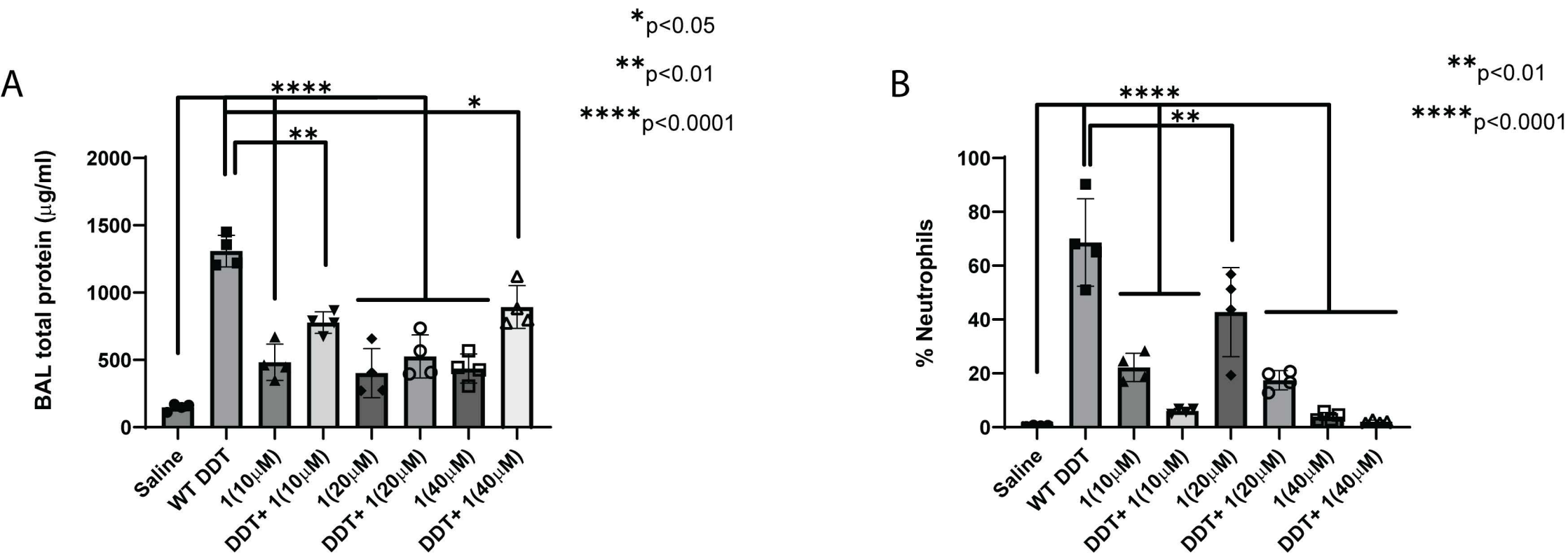
A
B
*p<0.05
**p<0.01
****p<0.0001
BAL total protein (μg/ml)
% Neutrophils
Saline
WT DDT
1(10μM)
DDT+ 1(10μM)
1(20μM)
DDT+ 1(20μM)
1(40μM)
DDT+ 1(40μM)

	D-DT-**1**
Data collection	
Space group	P 3
Cell dimensions	
a, *b*, *c* (Å)	83.72, 83.72, 40.63
α, β, γ (°)	90.00, 90.00, 120.00
Resolution (Å)	41.90 - 1.30(1.33-1.30) *
R_{sym} or R_{merge}	0.094(0.173)
$I / \sigma I$	20.3(8.6)
Completeness (%)	95.8(93.7)
Redundancy	6.7(6.2)
Refinement	
Resolution (Å)	41.90 -1.30
No. reflections	71400
R_{work} / R_{free}	0.12/0.16
No. atoms	
Protein	2638
Ligand/ion	49
Water	505
B-factors (Å^2)	
Protein	8.6
Ligand/ion	13.9
Water	26.6
R.m.s. deviations	
Bond lengths (Å)	0.012
Bond angles (°)	1.766

* Values in parentheses are for highest-resolution shell.

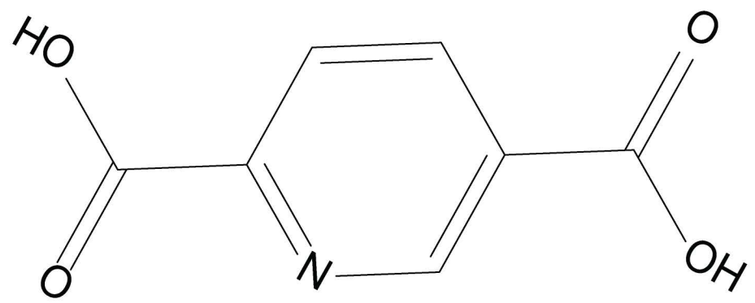

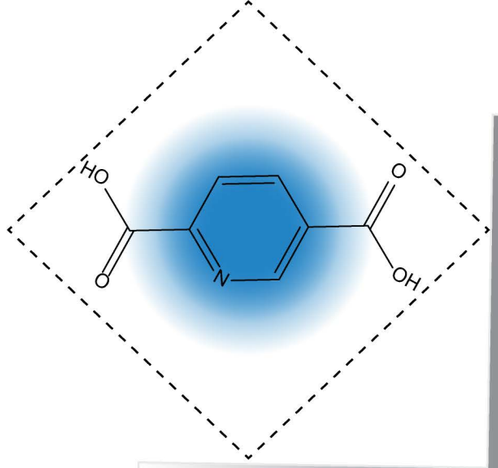

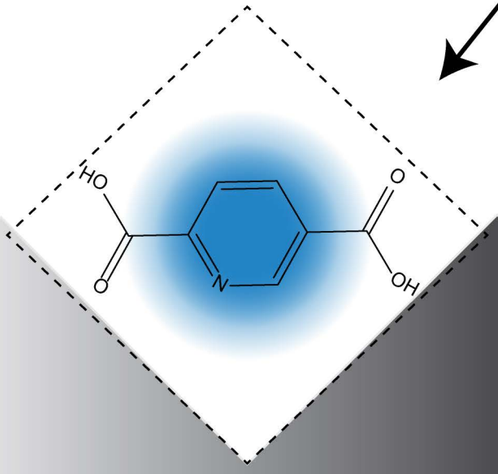

MIF

D-DT

79-fold selectivity

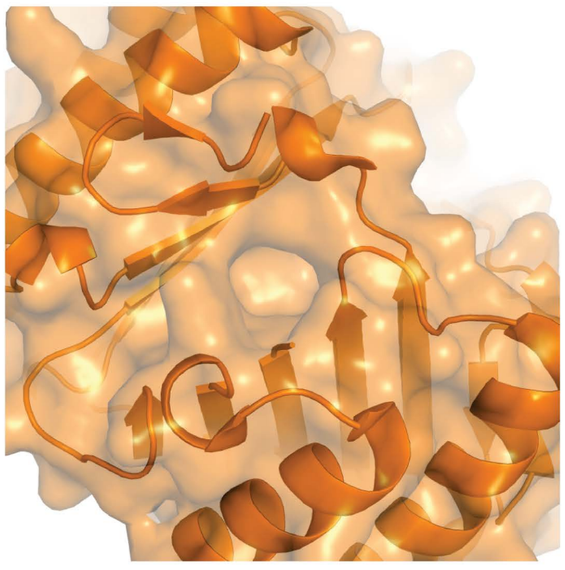

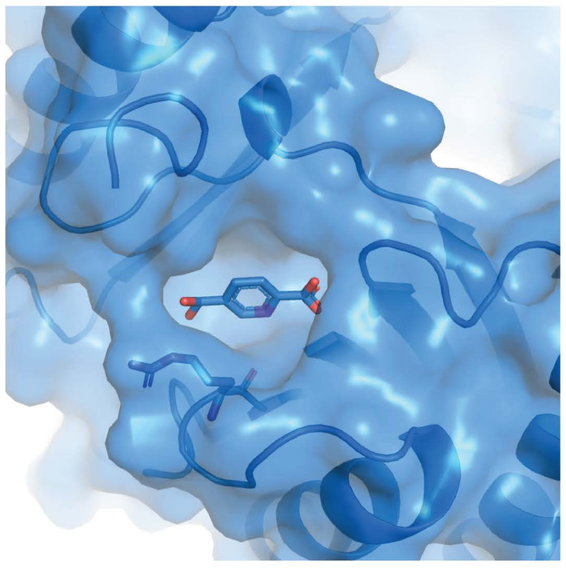

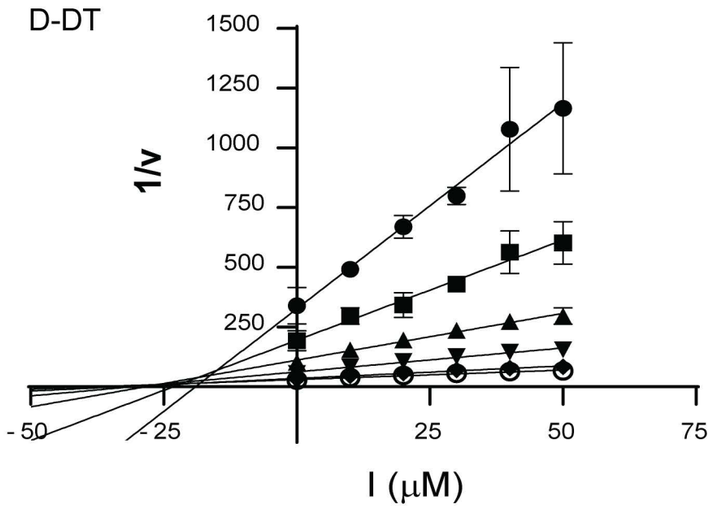

CD74 activation

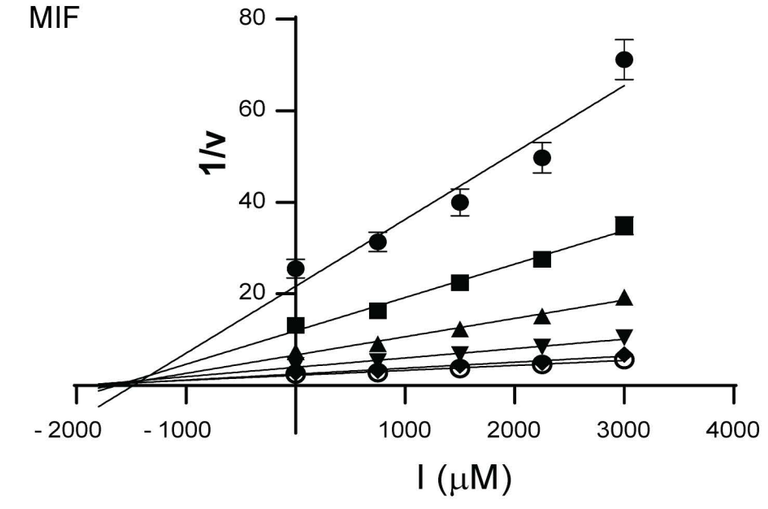

CD74 activation

Disease Progression